

University of Groningen

Relativity, correlation and core electron spectra

Klooster, Rob

IMPORTANT NOTE: You are advised to consult the publisher's version (publisher's PDF) if you wish to cite from it. Please check the document version below.

Document Version

Publisher's PDF, also known as Version of record

Publication date:

2015

[Link to publication in University of Groningen/UMCG research database](#)

Citation for published version (APA):

Klooster, R. (2015). Relativity, correlation and core electron spectra [Groningen]: University of Groningen

Copyright

Other than for strictly personal use, it is not permitted to download or to forward/distribute the text or part of it without the consent of the author(s) and/or copyright holder(s), unless the work is under an open content license (like Creative Commons).

Take-down policy

If you believe that this document breaches copyright please contact us providing details, and we will remove access to the work immediately and investigate your claim.

Downloaded from the University of Groningen/UMCG research database (Pure): <http://www.rug.nl/research/portal>. For technical reasons the number of authors shown on this cover page is limited to 10 maximum.

Relativity, correlation and core electron spectra

Rob Klooster

Cover image: NASA/JPL

Zernike Institute PhD series 2015-16

ISSN: 1570-1530

ISBN: 978-90-367-8100-8 (printed)

ISBN: 978-90-367-8099-5 (electronic)

The research presented in this thesis was performed in the research group Theoretical Chemistry of the Zernike Institute for Advanced Materials at the University of Groningen, The Netherlands.

Printed by CPI Koninklijke Wöhrmann



rijksuniversiteit
 groningen

Relativity, correlation and core electron spectra

Proefschrift

ter verkrijging van de graad van doctor aan de
 Rijksuniversiteit Groningen
 op gezag van de
 rector magnificus prof. dr. E. Sterken
 en volgens besluit van het College voor Promoties.

De openbare verdediging zal plaatsvinden op

vrijdag 16 oktober 2015 om 16.15 uur

door

Rob Klooster

geboren op 2 april 1983
 te Gorssel, Nederland

Promotor

Prof. dr. R. Broer

Beoordelingscommissie

Prof. dr. L. Visscher

Prof. dr. F. M. F. de Groot

Prof. dr. P. Rudolf

Contents

1	Introduction	1
2	Theory	9
2.1	Non-relativistic Theory	9
2.1.1	Hartree-Fock theory	10
2.1.2	Configuration interaction	12
2.1.3	Multi-configurational self-consistent field methods	13
2.1.4	Multi-configurational perturbation theory	14
2.2	Relativistic theory	18
2.2.1	Four-component methods	20
2.2.2	Two-component methods	21
2.2.3	Implementation of the Normalized Elimination of the Small Component	25
2.3	The embedded cluster model	28
2.3.1	<i>Ab initio</i> embedding model potentials	29
2.3.2	Extra-cluster relaxation	31
3	Theoretical Core Spectroscopy	33
3.1	Binding and excitation energies	34
3.2	Angular momentum coupling	35
3.3	Transition probabilities	36
3.4	The computational algorithms	40

4	Benchmark calculations on atomic uranium	43
4.1	Details of calculations	43
4.2	Results and discussion	45
4.3	Conclusions	49
5	Theoretical description of $L_{2,3}$ X-ray absorption in small titanium clusters	51
5.1	Computational details	51
5.2	Atomic titanium	53
5.3	Ti_2^+ molecule	54
5.3.1	Symmetry breaking and localization	57
5.4	Results and discussion	59
5.5	Conclusions	62
6	The 4p and 5p XPS of Ytterbium Phosphide	65
6.1	Details of calculations	65
6.2	Results and discussion	67
6.3	Conclusions	69
	Bibliography	71
	Samenvatting	79
	Acknowledgements	83
	Curriculum Vitae	85

Chapter 1

Introduction

The design of new (multi) functional materials is largely based on the knowledge of the microscopic properties of these materials. These properties are largely determined by the electronic structure: the electronic energy levels and associated electronic distributions. Core spectroscopies are valuable tools for the accurate determination of the electronic structure of atoms, molecules and solids.

In X-ray Photo-electron Spectroscopy (XPS) a high-energy, X-ray, photon is absorbed, leading to core electron ionization. Already half a century ago, Siegbahn and co-workers [1, 2] demonstrated that the core shell ionization energies depend on the environment of the ionized atom and the technique is still one of the most successful ones to characterize chemical compounds, for example on surfaces [3]. In chemistry, XPS is therefore also called Electron Spectroscopy for Chemical Analysis (ESCA) [4]. In X-ray absorption spectroscopy (XAS) a high-energy photon is absorbed, leading to excitation of a core electron rather than ionization. In both types of spectroscopy, XPS and XAS, a photon is absorbed. In contrast, Resonant Inelastic X-ray Scattering (RIXS) is a photon-in, photon-out spectroscopy. High energy photons lose part of their energy, they are inelastically scattered by the material. In Electron Energy Loss Spectroscopy (EELS) a material is exposed to a beam of electrons instead of photons. Some of the electrons undergo inelastic scattering, and the energy lost is, for example, used to ionize a core electron. Nowadays often a combination of more than one spectroscopy is used to characterize materials. For example, XPS and high resolution EELS have been used to analyze thin films of a benzylic amide macrocycle on gold [5]. This thesis focuses on core and deep valence excitation and ionization spectra by absorption of light, in particular on the analysis and prediction of XPS and XAS.

In XPS, the spectrum is obtained by irradiating the sample with a beam of monochromatic X-rays and measuring the kinetic energies and number of ionized electrons. The binding energy of an electron is the difference between the energy of the incident X-ray and its kinetic energy. The magnitude of the binding energy

of a core electron is largely determined by the energy needed to escape the electric field of the nuclear charge of the atom to which the electron is bound. Core binding energies are therefore very specific for the element and as such XPS (or ESCA) can be used in the analysis of the elemental composition of materials.

The binding energies do however change slightly, depending on the chemical environment and electronic state of the atom. The chemical shift, i.e. the change in binding energy compared to the free atom, gives detailed information about the electronic structure in the vicinity of the atom. A simple case is the change of the oxidation state of an atom: the binding energies of the core electrons of a positively charged atom will be higher than those of the neutral species. This can be explained by the different screening of the electric potential of the nucleus by the electrons in the system. Since the positively charged species contains less electrons, the screening will be lower, which results in an increased effective potential at the core shell and hence a higher binding energy.

Such a simple screening model ignores the explicit interaction of the created hole with the surrounding electrons. In most systems, a good description of these effects is of great importance for a detailed understanding of the spectrum. Accurate first-principles calculations can provide the important information of these interactions and can assist in the interpretation of experimental spectra. The need for accurate computational studies can be illustrated by an example [6]. It concerns the 3s XPS of crystalline NiO and MnO. Both spectra show a secondary peak at about 6 eV higher binding energy than the main peak. It is tempting to assume that the secondary peaks have a common origin. However, *ab initio* many-electron studies using embedded clusters revealed that in the case of NiO both peaks are associated with high spin final states, which both have considerable oxygen-to-metal charge transfer character, while in the case of MnO the contribution of charge transfer effects is much smaller and the secondary peak corresponds to a lower spin final state [7, 8]. Clearly, to obtain information about the electronic structures of transition metal oxides, XPS is a very powerful tool, especially when combined with theoretical analysis. Another well known successful example is the systematic analysis of the electronic structure of various iron-oxide films by Fe 2p core-level and valence-band spectra [9].

In XAS, the spectrum is obtained by measuring the absorption of X-rays as a function of wavelength. In contrast to XPS, the core electron is not ionized, but excited. The structure in the XAS close to the absorption edge is referred to as X-ray Absorption Near Edge Structure (XANES). The oscillatory structure at higher

energies is referred to as Extended X-ray absorption Fine Structure (EXAFS) and an alternative name for the lower energy structure is Near-Edge X-Ray Absorption Fine Structure (NEXAFS) [10]. This gives in general a richer spectrum than XPS, since not only the core shell is probed, but also the valence shell electronic structure. The interpretation of the XAS spectra may therefore be more difficult than in XPS.

One might naively think that core excitation spectra give only information on the excited states that are created in first instance. In reality, the spectra give also information on states that arise in response to the initial excitation and, moreover, on the unperturbed state that existed before the excitation. This can be nicely illustrated by the spectroscopic analysis of low-spin to high-spin transitions in particular iron coordination complexes, the so-called spin crossover complexes. Spin-crossover materials are transition metal based molecular systems that can remain for a long time in either one of two states, a low-spin and a high-spin state. Transitions between the states can be induced by changing the pressure, by heat, or by light. In order to spectroscopically analyse the spin crossover, use is made of a time-resolved spectroscopic technique, in this case femtosecond X-ray Absorption Near Edge Spectroscopy (XANES). See for example the work of Bressler and co-workers [11, 12]. The photo-ionization of an iron 1s electron by an intense hard X-ray pulse of femtosecond duration leads to X-ray fluorescence originating from the transition of a 3p electron to the 1s hole. The fluorescence of the sample is, with femtosecond resolution, monitored as a function of the time after the light flash and this gives direct information on the dynamics of the spin-crossover process.

The most accurate physical theory to describe systems on an atomic scale is quantum mechanics. It is based on the observation that all particles (electrons, nucleons, photons, etc.) exhibit both particle and wave properties (wave-particle duality). A system of a number of particles may then be described by the wave function $\Psi(\mathbf{x}, t)$, a function of the coordinates \mathbf{x} of all particles and time t . The time-dependent wave function is the solution to the equation¹

$$\hat{H}\Psi = i\frac{\partial}{\partial t}\Psi, \quad (1.1)$$

where \hat{H} is the Hamiltonian of the system. We may assume that the system before and after ionization or excitation is in a stationary state, such that the wave func-

¹All equations in this thesis are in atomic units, i.e. the reduced Planck's constant \hbar , the mass of the electron m_e , the elementary charge e and Coulomb's constant $1/(4\pi\epsilon_0)$ are all equal to unity.

tion may be separated into a time-dependent term and a term dependent only on the coordinates, $\Psi(\mathbf{x}, t) = \Psi(\mathbf{x})f(t)$. This leads to the equation for the time-independent wave function

$$\hat{H}\Psi(\mathbf{x}) = E\Psi(\mathbf{x}), \quad (1.2)$$

where E is the total energy of that state. Binding energies and excitation energies can be calculated by solving this equation for the initial state (before ionization/excitation) and the final state (after ionization/excitation) and taking the difference of the total energies.

The Hamiltonian \hat{H} contains all physical interactions in the system. When describing the states of the atomic core electrons, the inclusion of the effects of relativity in the Hamiltonian is mandatory, since relativity strongly modifies the atomic wave function near the nucleus and introduces a substantial energy shift into the electronic energy levels. It seems therefore natural to use the relativistic formalism based on the Dirac equation [13] to accurately calculate the core spectra [14, 15, 16, 17, 18, 19]. The four-component Dirac–Fock formalism [20, 21] is however considerably more complicated than the quantum chemical methods based on the non-relativistic formalism and can routinely be applied only to the calculation of relatively small systems. To describe the core spectra of large systems one needs to employ quantum chemical methods which have computational cost similar to the non-relativistic methods however provide accurate account of the relativistic effects. An economic approach is to start with non-relativistic orbitals and wave functions and add scalar relativistic corrections (the mass-velocity and Darwin terms) by modifying the one-electron Hamiltonian, while spin-orbit effects are included in a second step. These approximate approaches to include relativistic effects have the important practical advantage that standard quantum chemical program packages can be used.

In addition to relativity, electron–electron interactions also play an important role in the core electron spectra. Especially so-called dynamical and non-dynamical electron correlation effects complicate the theoretical treatment and the interpretation of the spectra. Hence, the experimental spectra can be interpreted and modeled by theory only if both relativity and electron correlation are accounted for. Moreover, to model the spectra, it is not sufficient to compute only energies, also good estimates of the relative intensities are required.

The importance of many-electron theories for electronic transition processes

in materials science has already been emphasized in a review by Adachi and Ogasawara [22]. A discussion using *ab initio* Green's function results for the XPS of several levels of atoms from calcium to uranium can be found in a review by Ohno [23]. Quantum theoretical methods to compute XPS and XAS have due to computational limitations mostly been limited to cases where the core hole is localized on one single atom. Moore and co-workers [24, 25, 26] combined relativistic atomic many-electron calculations [27], theoretical spin-orbit sum rules derived by Thole and Van der Laan [28, 29, 30, 31] with branching ratios observed in XAS and EELS to obtain valence spin-orbit interactions in transition metal, lanthanide and actinide materials. Bagus and co-workers carried out *ab initio* quantum theoretical studies of XPS spectra of (cation) core levels in oxides [14, 16, 32, 33, 34, 35, 36, 37] using clusters of atoms representing the bulk of the solid. They also performed theoretical XPS surface and chemisorption studies using clusters of atoms representing the chemisorbed species and a (small) portion of the substrate [38, 39, 40, 41, 42]. These studies use configuration interaction (CI) wave functions to represent the many-electron effects, and the orbitals are determined in a Hartree-Fock calculation. For a recent review of the concepts needed for the correct analysis of XPS features, see [43], where the significance of combining theory and experiment is shown by discussions of the physical and chemical origins of the XPS features for a variety of molecular and condensed phase materials. Recently, Josefsson and co-workers [44, 45] presented the results for L-edge XAS and RIXS spectra of an *ab initio* computational scheme based on second order perturbation theory, RASPT2 with the orbitals obtained from a Restricted Active Space Self Consistent Field (RASSCF) calculation. A CI wave function was used in the semi-empirical methods based on the Anderson Model employed to describe XPS spectra [46, 47, 48]. It is also possible to use Kohn-Sham DFT orbitals as a basis for the CI wave functions. Such calculations have been carried out for XAS of transition metal compounds by Ikeno et al. [49, 50, 51]. Recently, Barysz and Syrocki [52] reported relativistic calculations to study the X-ray photoelectron spectra of noble gases, applying an infinite-order two-component (IOTC) method for scalar relativistic effects [53], while effect of spin-orbit coupling was introduced via restricted active space interaction (RASSI). For the deep core energies the discrepancies between the experimental and calculated values were still found to be rather large, mainly due to quantum electrodynamic effects.

In this thesis we develop an approach for the calculation of core spectra, which

uses the normalized elimination of the small component (NESC) method [54]. When applied in the one-component form [55], this method enables one to treat very large molecular systems. The one-component form is however missing the important relativistic effect of spin–orbit coupling. Spin–orbit coupling is reintroduced in the formalism via the restricted active space state interaction (RASSI) method [56], using the atomic mean-field SO integrals (AMFI) [57].

Chapter 2 of this thesis gives a detailed overview of the theory and the various computational methods used to calculate initial and final states and their energies. A high level treatment of both relativistic and electron correlation effects is realized by combining the NESC method with the complete active space SCF method (CASSCF) into many-electron wave functions. The binding/excitation energy of a final state is however only one of the parameters used to model the spectra, the other is the transition intensity, a measure of the height of the peaks in the spectrum. This is proportional to the probability that a transition can be made from the initial state to the final state. For excitations, it is proportional to the transition dipole moment between the initial and final state, as in other excitation spectroscopies. For ionizations, the intensity of the XPS spectral lines is treated within the sudden approximation [58]. The sudden approximation is exact for infinitely large photon energy and provides accurate relative intensities for photon energies which are about 100–200 eV above the ionization threshold [59]. In the sudden approximation the transition probability is related to the overlap of the final state wave function with a "frozen" final state wave function, i.e. the initial state wave function with an electron removed from the core orbital of interest. The derivation of the sudden approximation for CASSCF type wave functions and the algorithm to compute overlaps between spin–orbit coupled wave functions is a very important and time-consuming step in the development of our method for the calculation of XPS spectra. An overview of X-ray absorption and photoelectron spectroscopy, in particular how transition intensities are determined, is given in chapter 3.

In chapter 4 we benchmark the developed method in the calculation of the 4f XPS of the U^{5+} ion. For this system, the results of accurate four-component calculations are available to which the calculated binding energies and relative transition intensities are compared. We show how the final states can be interpreted in terms of the balance between angular momentum coupling and spin–orbit coupling. Also the effects of configuration interaction and orbital relaxation on the binding energies and transition intensities is studied.

In chapter 5, we apply the method to the calculation of the 2p XAS of the

Ti atom and the Ti^+ and Ti_2^+ ions. The description of the dimer is of particular interest, since it involves the calculation of the core-excited states of a non-centrosymmetric system. The consequences of the core excitation with respect to the symmetry of the final state wave functions are explained in detail. The results of these calculations are compared to the experimental 2p XAS of size-selected titanium clusters [60]. The nature of the anomalous branching ratio — the deviation from the statistical ratio between the intensities of the main peaks — is studied. This includes the variation of the speed of light in the calculation to enhance relativistic effects.

The Yb 4p and 5p XPS spectra of ytterbium phosphide YbP are investigated in chapter 6 using the developed method and compared to the experimental spectrum [61]. These calculations are performed in the embedded cluster approximation to describe the crystal environment. By explicitly including a shell of ligand P atoms in the calculation, the importance of the inclusion of ligand-to-metal charge transfer excitations in the calculations can be analyzed.

Chapter 2

Theory

2.1 Non-relativistic Theory

Any theory describing stationary quantum states in the non-relativistic limit is based on the Schrödinger equation,

$$\hat{H}\Psi = E\Psi. \quad (2.1)$$

The Hamiltonian operator \hat{H} contains information about all interactions in the system. Usually the Born-Oppenheimer (BO) approximation is assumed, which states that, since nuclei are a factor 10^3 – 10^5 heavier than electrons, the electrons instantaneously adapt to any changes in nuclear positions. The BO electronic Hamiltonian is

$$\hat{H} = -\sum_i \frac{1}{2} \nabla_i^2 - \sum_{\mu,i} \frac{Z_\mu}{|\mathbf{R}_\mu - \mathbf{r}_i|} + \sum_{i<j} \frac{1}{|\mathbf{r}_i - \mathbf{r}_j|} + \sum_{\mu<\nu} \frac{Z_\mu Z_\nu}{|\mathbf{R}_\mu - \mathbf{R}_\nu|}, \quad (2.2)$$

and contains (from left to right) the electronic kinetic energy term, the electron–nucleus, electron–electron and the nucleus–nucleus interactions. The electronic wave function Ψ now depends not only on the electron coordinates, but also parametrically on the nuclear coordinates $\{\mathbf{R}_\mu\}$, which means that for every nuclear configuration a new wave function has to be computed.

It can be shown that the expectation value of the energy for any wave function is always higher than the lowest energy E_0 of the exact solution of the Schrödinger equation Ψ_0 ,

$$\frac{\langle \Psi | \hat{H} | \Psi \rangle}{\langle \Psi | \Psi \rangle} > E_0. \quad (2.3)$$

Also, the closer the wave function is to the exact ground state wave function, the

lower the energy expectation value is. The variational principle states that the “best” wave function can be found by varying the wave function until the energy is at a minimum.

2.1.1 Hartree-Fock theory

The many-body wave function must obey the Pauli principle, which states that it must be anti-symmetric under the exchange of the coordinates of any two electrons. A simple *ansatz* of an approximate wave function with this property can be constructed by assuming that individual electrons are described by one-electron wave functions ψ , called spin-orbitals. The spin-orbital occupied by electron i depend on four coordinates, three spatial coordinates and one “coordinate” describing spin: $\psi(\mathbf{r}_i, s_i)$. In the following we will use the shorthand notation $\psi(\mathbf{x}_i)$. The simplest anti-symmetric N -body wave function can then be written as a Slater determinant,

$$\Psi(\mathbf{x}_1, \dots, \mathbf{x}_N) = \frac{1}{\sqrt{N!}} \begin{vmatrix} \psi_1(\mathbf{x}_1) & \psi_1(\mathbf{x}_2) & \cdots & \psi_1(\mathbf{x}_N) \\ \psi_2(\mathbf{x}_1) & \psi_2(\mathbf{x}_2) & \cdots & \psi_2(\mathbf{x}_N) \\ \vdots & \vdots & \ddots & \vdots \\ \psi_N(\mathbf{x}_1) & \psi_N(\mathbf{x}_2) & \cdots & \psi_N(\mathbf{x}_N) \end{vmatrix}, \quad (2.4)$$

built from a set of N normalized and mutually orthogonal spin-orbitals ψ , with $\langle \psi_i | \psi_j \rangle = \delta_{ij}$. Exchange of two particles is equivalent to the exchange of two columns in the determinant and gives the original wave function with a minus sign, which therefore obeys the Pauli principle.

Minimization of the energy expectation value with this choice of wave function yields the general Hartree-Fock (HF) equations for the spin-orbitals

$$\hat{F}\psi_i(\mathbf{x}) = \sum_j \epsilon_{ij} \psi_j(\mathbf{x}), \quad (2.5)$$

where the summation runs over the “occupied” spin-orbitals, i.e. the spin-orbitals in the Slater determinant (Eq. 2.4) and the one-electron Fock operator \hat{F} is defined as

$$\hat{F} = \hat{h} + \hat{J} - \hat{K}. \quad (2.6)$$

Here, the one-electron part of this effective one-electron Hamiltonian is denoted

as \hat{h} . The Coulomb (\hat{J}) and exchange (\hat{K}) operators are defined by their action on an arbitrary function of electron 1 as

$$\hat{J}f(\mathbf{x}_1) = \sum_i \left[\int \frac{\psi_i^*(\mathbf{x}_2)\psi_i(\mathbf{x}_2)}{r_{12}} d\mathbf{x}_2 \right] f(\mathbf{x}_1) \quad (2.7)$$

$$\hat{K}f(\mathbf{x}_1) = \sum_i \left[\int \frac{\psi_i^*(\mathbf{x}_2)f(\mathbf{x}_2)}{r_{12}} d\mathbf{x}_2 \right] \psi_i(\mathbf{x}_1), \quad (2.8)$$

where the summations run over the occupied spin-orbitals. It can be seen that \hat{J} describes the classical Coulomb interaction with the electric field generated by $\rho = \sum_i \psi_i^* \psi_i$, the total electron density. The operator \hat{K} looks similar, except that (in the right-hand side of Eq. 2.8) the coordinates of electron 1 and 2 are exchanged between ψ_i and f . This exchange interaction is a direct consequence of the anti-symmetry of the many-electron wave function and has no classical analogue.

There is considerable freedom in the choice of spin-orbitals since any unitary transformation of the spin-orbitals leaves the Slater determinant unchanged. Therefore it is common to choose the spin-orbitals in such a way that the matrix of ϵ_{ij} becomes diagonal. This yields the *canonical* Hartree-Fock equations:

$$\hat{F}\psi_i(\mathbf{x}) = \epsilon_i \psi_i(\mathbf{x}). \quad (2.9)$$

The diagonal element ϵ_i is the orbital energy of ψ_i . The complicated many-body Schrödinger equation is now reduced to a system of one-electron equations, which are coupled via the Coulomb and exchange operators. This system has to be solved self-consistently, so that the solutions to the Hartree-Fock equations describe the same (Coulomb, exchange) field as was used in the calculation. This method has therefore been termed the Self-Consistent Field (SCF) method.

Generally, the spin-orbitals can be written as a product of a spatial part φ (called an *orbital*) and a spin part,

$$\begin{aligned} \psi_k(\mathbf{x}) &= \varphi_k(\mathbf{r})\alpha(s) \\ \psi_l(\mathbf{x}) &= \varphi_l(\mathbf{r})\beta(s), \end{aligned} \quad (2.10)$$

for a spin-up and spin-down electron, respectively. In closed shell molecules, the electrons are paired with opposite spin in orbitals of the same spatial extent, i.e. for these two paired spin-orbitals $\varphi_k = \varphi_l$. This property is used in Restricted

Hartree-Fock (RHF), where the spatial part of pairs of spin-orbitals are restricted to be the same.

In order to solve the system of equations, the orbitals are expanded in a set of (usually) atom-centered basis functions, as

$$\varphi_i(\mathbf{r}) = \sum_j C_{ji} \chi_j(\mathbf{r}). \quad (2.11)$$

Substitution into Eq. 2.9, premultiplying with χ_k^* and integrating yields

$$\left\langle \chi_k \left| \hat{F} \right| \sum_j C_{ji} \chi_j \right\rangle = \left\langle \chi_k \left| \sum_j C_{ji} \chi_j \right\rangle \epsilon_i \quad (2.12)$$

$$\sum_j F_{kj} C_{ji} = \sum_j S_{kj} C_{ji} \epsilon_i \quad (2.13)$$

$$\mathbf{FC} = \mathbf{SC}\epsilon \quad (2.14)$$

This matrix equation is called the Roothaan-Hall equation [62, 63]. The matrix representation of the the Fock operator \mathbf{F} has elements $F_{kj} = \langle \chi_k | \hat{F} | \chi_j \rangle$. The overlap matrix \mathbf{S} has elements $S_{kj} = \langle \chi_k | \chi_j \rangle$ equal to the overlap of basis functions k and j . The vector ϵ contains all orbital energies ϵ_i . This equation can be solved numerically for the coefficients and energies using matrix techniques.

2.1.2 Configuration interaction

The Hartree-Fock wave function is based on the mean field approximation. The wave function ansatz implies that the electrons are moving in the field of the nuclei and the *average* field of the other electrons. The instantaneous reaction to the motion of the other electrons is neglected, which is often called the neglect of electron correlation. Depending on the system, this may be a serious approximation, leading even to qualitatively incorrect results.

The effects of electron correlation can be included, starting from the HF wave function, by Configuration Interaction (CI). Instead of using a single Slater determinant, the wave function is approximated by a linear combination of determinants

$$\Psi = c_0 \Psi_0 + \sum_{ir} c_{ir} \Psi_i^r + \sum_{ijrs} c_{ijrs} \Psi_{ij}^{rs} + \dots \quad (2.15)$$

Here, the HF reference Ψ_0 is complemented by a series of “excited” determinants. The singly excited determinants Ψ_i^r are equal to the HF reference, but with an electron excited from occupied orbital i to unoccupied, virtual, orbital r . Virtual spin-orbitals are those spin-orbitals that form, together with the occupied spin-orbitals, a complete orthonormal set. Doubly excited determinants $\Psi_{ij}^{r,s}$ involve excitations from orbitals i to r and j to s .

The HF reference together with all possible (up to N -fold) excitations, constitute a complete set. This means that every possible N -electron wave function (within a certain basis set) can be written as the expansion in Eq. 2.15. This is in particular the case for the exact ground state wave function. When all possible excitations are taken into account, this is referred to as the Full CI limit.

For systems with more than a few electrons, the number of determinants grows quickly out of hand. In practical calculations, the CI expansion is usually truncated after e.g. all single and double excitations have been included. It may be tempting to truncate the series after only the single excitations have been included. Brillouin’s theorem [64] states however that mixing singly excited determinants with the HF determinant is equivalent to applying orbital rotations, hence no energy lowering can occur compared to a fully optimized HF wave function. So in order for CI to be useful, at least doubly excited determinants should be present in the CI expansion.

A major problem with such a truncated CI expansion is however the lack of size-extensivity, which means that the energy does not scale linearly with the number of electrons in the system. There are several ways to truncate the CI expansion in such a way as to keep the size-extensivity. An important one is Coupled Cluster (CC) theory, where the wave function is defined as an exponential expansion, instead of the linear expansion in CI. This allows for a truncation that is both manageable computationally and size-extensive. To use CC theory to calculate highly excited states like those involved in core excitations is however not yet practical.

2.1.3 Multi-configurational self-consistent field methods

In Configuration Interaction, the orbitals which are used to define the Slater determinants are the same as in the Hartree-Fock calculation. We can expand the formalism by allowing not only the CI coefficients (in Eq. 2.15) to be optimized, but also the orbital coefficients (in Eq. 2.11). This is called the Multi-configurational

Self-consistent field (MCSCF) method. Because of the increased freedom in the definition of the wave function, the number of determinants in an MCSCF expansion can be relatively small compared to CI.

A way to limit the number of determinants in the MCSCF expansion is to allow all excitations, but only in a subset of the orbitals. The orbitals are split into three sets: the inactive orbitals are doubly occupied in all determinants, the active orbitals (or active space) may have any occupation and the virtual orbitals stay unoccupied in all determinants. A number of electrons (the active electrons) are distributed over the active space in all possible ways. This is the Complete Active Space SCF method (CASSCF).

It is possible to restrict the excitations which are included in the MCSCF expansion even more by splitting the active space into three spaces. The first (RAS1) includes orbitals which are mostly doubly occupied, but may have a maximum number of holes. The second (RAS2) is equivalent to the active space in CASSCF, i.e. all occupations are allowed. The third space (RAS3) includes orbitals which are mostly unoccupied, but may have a maximum number of electrons. This Restricted Active Space SCF (RASSCF) method is very versatile, since the wave function expansion can be equivalent to that of previously mentioned methods by choosing the active space in specific ways.

In the specific case of core-excited or -ionized states, the RASSCF method is especially useful. When the valence orbitals are put in the RAS2 space, the core orbitals may then be chosen to belong to the RAS1 or RAS3 space. In general, the best choice is to put the n_c core orbitals in the RAS3 space and allow at most $2n_c - 1$ electrons in this space. This will ensure that the lowest states are those states which have a single core-hole. A drawback is that all (up to $2n_c$ -fold) excitations from the core orbitals are included in the CI expansion and, even though they contribute negligibly to the wave function, the number of determinants may become too large. If that is the case, a better choice would be to put the core orbitals in the RAS1 space and allow up to one hole in this space. The disadvantage is that the lowest states are states without a core-hole, which complicates the calculations.

2.1.4 Multi-configurational perturbation theory

The MCSCF methods were designed for those systems where a single-determinant HF wave function gives a qualitatively wrong result. This is usually the case when

there are excited configurations, with a comparable energy expectation value as the HF ground state energy, which can contribute to the ground state MCSCF wave function. This *static* electron correlation is accounted for by the MCSCF methods, but the remainder (i.e. *dynamical* electron correlation) is neglected because of the truncation of the CI expansion. Part of the dynamical electron correlation can be recovered by applying perturbation theory to the MCSCF wave function.

The assumption made in Rayleigh-Schrödinger perturbation theory is that the exact Hamiltonian can be split into a zeroth order term and a *small* perturbation with strength λ as

$$\hat{H} = \hat{H}_0 + \lambda\hat{H}_1. \quad (2.16)$$

The wave function and energy are expanded in a similar way

$$\Psi = \Psi^{(0)} + \lambda\Psi^{(1)} + \lambda^2\Psi^{(2)} + \dots \quad (2.17)$$

$$E = E^{(0)} + \lambda E^{(1)} + \lambda^2 E^{(2)} + \dots \quad (2.18)$$

where it is assumed that the zeroth order wave functions and energies, the exact solutions to the zeroth order Schrödinger equation,

$$\hat{H}_0\Psi^{(0)} = E^{(0)}\Psi^{(0)}, \quad (2.19)$$

can be computed. By solving the system of equations and collecting different powers of λ , we get, up to second order

$$\hat{H}_0 \left| \Psi^{(0)} \right\rangle = E^{(0)} \left| \Psi^{(0)} \right\rangle, \quad (2.20)$$

$$\left(\hat{H}_0 - E^{(0)} \right) \left| \Psi^{(1)} \right\rangle = \left(E^{(1)} - \hat{H}_1 \right) \left| \Psi^{(0)} \right\rangle, \quad (2.21)$$

$$\left(\hat{H}_0 - E^{(0)} \right) \left| \Psi^{(2)} \right\rangle = \left(E^{(1)} - \hat{H}_1 \right) \left| \Psi^{(1)} \right\rangle + E^{(2)} \left| \Psi^{(0)} \right\rangle. \quad (2.22)$$

The set of eigenfunctions of H_0 ($\Psi_i^{(0)}$) form a complete orthogonal set and may be used to expand the first order wave function as

$$\Psi_i^{(1)} = \sum_j a_{ji}^{(1)} \Psi_j^{(0)} \quad (2.23)$$

We derive the following expressions for the correction to the energy up to second

order:

$$E^{(0)} = \langle \Psi^{(0)} | \hat{H}_0 | \Psi^{(0)} \rangle, \quad (2.24)$$

$$E^{(1)} = \langle \Psi^{(0)} | \hat{H}_1 | \Psi^{(0)} \rangle, \quad (2.25)$$

$$E^{(2)} = \langle \Psi^{(0)} | \hat{H}_1 | \Psi^{(1)} \rangle. \quad (2.26)$$

The first order correction to the wave function is defined in terms of the expansion coefficients as $a_{ii}^{(1)} = 1$ and for $i \neq j$:

$$a_{ji}^{(1)} = \frac{\langle \Psi_j^{(0)} | \hat{H}_1 | \Psi_i^{(0)} \rangle}{E_j^{(0)} - E_i^{(0)}} \quad (2.27)$$

In Møller-Plesset perturbation theory, the zeroth order Hamiltonian is chosen to be the sum of one-electron Fock operators

$$\hat{H}_0 = \sum_i^N \hat{F}(i) \quad (2.28)$$

The ground state HF wave function is then the reference function, $\Psi_0^{(0)}$. The ground state energy $E_0^{(0)}$ plus the first order energy correction $E_0^{(1)}$ sum up to the Hartree-Fock energy in this case, so in order to get an improved description of electron correlation, at least the second order energy correction needs to be calculated. The first order wave function can be expanded in terms of doubly excited determinants (because of Brillouin's theorem), compare Eq. 2.15, as

$$\Psi_1 = \sum_{i>j, a>b} C_{ijab} \Psi_{ij}^{ab}, \quad (2.29)$$

where i and j are occupied and a and b virtual spin-orbitals. The expansion coefficients and the second order energy can be found following Eqs. 2.21 and 2.26

as

$$C_{ijab} = -\frac{\langle \Psi_0 | \hat{H} | \Psi_{ij}^{ab} \rangle}{\epsilon_a + \epsilon_b - \epsilon_i - \epsilon_j} \quad (2.30)$$

$$E_2 = -\frac{\left| \langle \Psi_0 | \hat{H} | \Psi_{ij}^{ab} \rangle \right|^2}{\epsilon_a + \epsilon_b - \epsilon_i - \epsilon_j} \quad (2.31)$$

In CASPT2 theory, the reference wave function is chosen to be the CASSCF wave function and the difference compared to the full CI wave function is considered a perturbation. The full CI configuration space can be decomposed into four subspaces: the CASSCF reference (V_0), the orthogonal complement to the CASSCF reference in the same CAS space (V_K), the space containing all single and double excitations from the inactive and active space (of the reference wave function) to the virtual space (V_{SD}) and all higher order excitations (V_X). The hamiltonian \hat{H}_0 is constructed in such a way that an eigenfunction is the CASSCF reference,

$$\hat{H}_0 = \hat{P}_0 \hat{F} \hat{P}_0 + \hat{P}_K \hat{F} \hat{P}_K + \hat{P}_{SD} \hat{F} \hat{P}_{SD} + \hat{P}_X \hat{F} \hat{P}_X. \quad (2.32)$$

The operator $\hat{P}_S = (|\Psi_S\rangle \langle \Psi_S|)$ is the projection operator onto subspace V_S , i.e. one of V_0 , V_K , V_{SD} or V_X . The Fock operator (\hat{F}) is defined, like HF theory (eq. 2.6), as a one-electron operator

$$\hat{F} = \sum_{p,q} \hat{f}_{pq} \hat{E}_{pq}, \quad (2.33)$$

with E_{pq} the spin-averaged excitation operator. The difference to the HF Fock operator is that in general the matrix f_{pq} is not diagonal, but has a 3×3 block diagonal structure corresponding to the three orbital subspaces (inactive, active and virtual). The matrix can be simplified by diagonalizing each block separately, since the CAS CI space is invariant to such a transformation. However the consequence is that the off-diagonal blocks are not zero anymore, i.e. the equation $\hat{f}_{pq} = \epsilon_p \delta_{pq}$ only holds when orbitals p and q belong to the same subspace. After diagonalization, the Fock operator has the following form:

$$\hat{F} = \sum_p \epsilon_p \hat{E}_{pp} + \sum_{i,t} \hat{f}_{it} (\hat{E}_{it} + \hat{E}_{ti}) + \sum_{t,a} \hat{f}_{ta} (\hat{E}_{ta} + \hat{E}_{at}), \quad (2.34)$$

where the indices p run over all orbitals, i over the inactive orbitals, t over the active orbitals and a over the virtual orbitals.

In order to construct the first-order wave function Ψ_1 , only those configurations which interact directly with the reference CASSCF need to be included in the expansion, i.e. only those that belong to the V_{SD} space. The first order wave function is then

$$\Psi_1 = \sum_{p,q,r,s} C_{pqrs} |pqrs\rangle \quad (2.35)$$

$$|pqrs\rangle = \hat{E}_{pq}\hat{E}_{rs} |\Psi_0\rangle \quad (2.36)$$

The expansion coefficients can be found by solving the matrix equation

$$(\mathbf{F} - E_0\mathbf{S})\mathbf{C} = -\mathbf{V}, \quad (2.37)$$

where \mathbf{F} is the matrix representation of the Fock operator in the V_{SD} space, \mathbf{S} the corresponding overlap matrix, \mathbf{C} the vector of coefficients C_{pqrs} and \mathbf{V} the vector representing the interaction between the reference function and V_{SD} , with elements $V_{pqrs} = \langle \Psi_0 | \hat{H} | pqrs \rangle$.

This equation suffers from linear dependencies, which have to be removed before it can be solved. When the coefficients have been calculated, the second order correction to the energy can easily be found, according to Eq. 2.26, by

$$E_2 = \langle \Psi_0 | \hat{H}_1 | \Psi_1 \rangle = \mathbf{V}^\dagger \mathbf{C} \quad (2.38)$$

2.2 Relativistic theory

In the theory described so far, the effects of (special) relativity have been completely neglected. These effects are however important in the treatment of the valence electronic structure of heavy elements, as well as the core electronic structure of practically all elements.

The effects of special relativity are included in the quantum theory by the Dirac

equation, which is for a single electron in a potential V

$$\hat{H}_D \Psi = E \Psi \quad (2.39)$$

$$\hat{H}_D = \beta mc^2 + c \boldsymbol{\alpha} \cdot \mathbf{p} + V. \quad (2.40)$$

The factors β and $\boldsymbol{\alpha} = (\alpha_x, \alpha_y, \alpha_z)$ are defined such that they anticommute with each other. This is achieved by expressing them as 4×4 matrices.

$$\beta = \begin{pmatrix} \mathbf{I}_2 & \mathbf{0}_2 \\ \mathbf{0}_2 & -\mathbf{I}_2 \end{pmatrix} \quad (2.41)$$

$$\boldsymbol{\alpha} = \begin{pmatrix} \mathbf{0}_2 & \boldsymbol{\sigma} \\ \boldsymbol{\sigma} & \mathbf{0}_2 \end{pmatrix}, \quad (2.42)$$

with the Pauli matrices $\boldsymbol{\sigma} = (\sigma_x, \sigma_y, \sigma_z)$ defined as

$$\sigma_x = \begin{pmatrix} 0 & 1 \\ 1 & 0 \end{pmatrix}, \quad \sigma_y = \begin{pmatrix} 0 & -i \\ i & 0 \end{pmatrix}, \quad \sigma_z = \begin{pmatrix} 1 & 0 \\ 0 & -1 \end{pmatrix}. \quad (2.43)$$

This has the consequence that Ψ must be a four-component wave function, usually grouped in two components as

$$\Psi = \begin{pmatrix} \psi^L \\ \psi^S \end{pmatrix}. \quad (2.44)$$

The energy spectrum of the Dirac equation with an attractive potential V has three main features. The electronic solutions can be split into the bound states with energies $E < mc^2$ and a positive energy continuum at energies $E > mc^2$. The positronic solutions form a negative energy continuum at $E < -mc^2$. The large component of the wave function ψ^L is large, while the small component ψ^S is small for electronic solutions. For positronic solutions ψ^L is small and ψ^S large.

The existence of the negative energy continuum may seem unphysical, since an electron in any state could keep decaying and release an infinite number of photons. It is therefore assumed that all negative energy states are filled and additional electrons may only occupy the positive energy states. The infinite negative charge of the so-called Dirac sea of electrons is compensated by an equal positive charge. A hole in the negative energy states is then interpreted as a positron, and electron-positron pairs can be formed by an excitation from a negative energy

state to a positive energy state.

The rest mass energy of the electron is usually subtracted in the Dirac equation,

$$\begin{pmatrix} V & c\boldsymbol{\sigma} \cdot \mathbf{p} \\ c\boldsymbol{\sigma} \cdot \mathbf{p} & V - 2mc^2 \end{pmatrix} \begin{pmatrix} \psi^L \\ \psi^S \end{pmatrix} = E \begin{pmatrix} \psi^L \\ \psi^S \end{pmatrix} \quad (2.45)$$

2.2.1 Four-component methods

The inclusion of relativity has the largest effect on the one-electron part of the interactions. The two-electron interactions are also modified by relativity, but these effects are small and are often ignored. Therefore, as a start, we take the same Coulomb term as in the non-relativistic theory to describe the two-electron interaction. The Breit interaction may be added to include at least part of the relativistic effects into the two-electron term,

$$\hat{B}_{ij} = -\frac{1}{2|\mathbf{r}_{ij}|} \left(\boldsymbol{\alpha}_i \cdot \boldsymbol{\alpha}_j + \frac{(\boldsymbol{\alpha}_i \cdot \mathbf{r}_{ij})(\boldsymbol{\alpha}_j \cdot \mathbf{r}_{ij})}{|\mathbf{r}_{ij}|^2} \right), \quad (2.46)$$

with $\mathbf{r}_{ij} = \mathbf{r}_i - \mathbf{r}_j$. The Breit interaction includes an unretarded and a retarded magnetic interaction. A large part of the Breit interaction can be included by taking just the unretarded magnetic interaction, i.e. the Gaunt interaction,

$$G_{ij} = -\frac{\boldsymbol{\alpha}_i \cdot \boldsymbol{\alpha}_j}{|\mathbf{r}_{ij}|}. \quad (2.47)$$

This avoids having to calculate the complicated second term in the Breit interaction.

The Dirac-Fock method combines the non-relativistic Hartree-Fock method with the relativistic Dirac Hamiltonian. The wave function is again approximated by a Slater determinant, now in a basis of four-component spin-orbitals. The large and small components of the orbitals are expanded, each in their own basis set.

$$\psi_i^L = \sum_{\mu} A_{\mu i} g_{\mu} \quad \psi_i^S = \sum_{\mu} B_{\mu i} f_{\mu} \quad (2.48)$$

By just freely optimizing the wave function, the energy would drop into the negative energy continuum. This can be prevented by choosing the basis set in a proper way, by the so-called restricted kinetic balance. The large component basis set

$\{g_\mu\}$ is chosen in a similar manner as in the non-relativistic theory. For every large component basis function, a small component basis function is then calculated by

$$f_\mu = \frac{1}{2mc} \boldsymbol{\sigma} \cdot \mathbf{p} g_\mu. \quad (2.49)$$

The restricted balance condition can be included in the formalism, leading to the Dirac equation in matrix form

$$\begin{pmatrix} \mathbf{V} & \mathbf{T} \\ \mathbf{T} & \mathbf{W} - \mathbf{T} \end{pmatrix} \begin{pmatrix} \mathbf{A} \\ \mathbf{B} \end{pmatrix} = \begin{pmatrix} \mathbf{S} & 0 \\ 0 & (2mc^2)^{-1} \mathbf{T} \end{pmatrix} \begin{pmatrix} \mathbf{A} \\ \mathbf{B} \end{pmatrix} \mathbf{E} \quad (2.50)$$

Here, we have used the identity $(\boldsymbol{\sigma} \cdot \mathbf{p})(\boldsymbol{\sigma} \cdot \mathbf{p}) = p^2 = 2m\hat{T}$, where \hat{T} is the non-relativistic kinetic energy operator. The matrix \mathbf{W} is the matrix representation of $(4m^2c^2)^{-1}(\boldsymbol{\sigma} \cdot \mathbf{p})V(\boldsymbol{\sigma} \cdot \mathbf{p})$. This is the only matrix in the equation which is not a diagonal 2×2 matrix. Therefore, all spin-dependence is due to this term. It can be split into a spin-free and spin-dependent part using the Dirac relation

$$(\boldsymbol{\sigma} \cdot \mathbf{p})V(\boldsymbol{\sigma} \cdot \mathbf{p}) = \mathbf{p}V \cdot \mathbf{p} + i\boldsymbol{\sigma} \cdot (\mathbf{p}V \times \mathbf{p}). \quad (2.51)$$

In order to get a spin-free formalism, the second term must be discarded. In that case, spin-orbit effects are completely ignored. These can however be included after the SCF part of the calculation, as we will discuss in section 2.2.3.

From equation (2.50), it is easy to take the non-relativistic limit. The second row gives the relation between the coefficients of the small and large components: $\mathbf{A} = \mathbf{B}$. Consequently the small component becomes zero, since the basis functions of the small component tend to zero in the non-relativistic limit. The first row reduces to the Schrödinger equation in matrix form, $(\mathbf{V} + \mathbf{T})\mathbf{A} = \mathbf{S}\mathbf{A}\mathbf{E}$.

2.2.2 Two-component methods

The four-component methods, as described above, are computationally very expensive. Several attempts have been made to simplify the equations, the most important ones of which we shall discuss here. The main problem in the four-component methods is the calculation of the small component. When a basis set in terms of contracted Gaussians is used, the number of primitive basis functions for the small component as calculated from the restricted kinetic balance is about twice the number for the large component. Since the small component is of minor

importance compared to the large component, it makes sense to find approximations for it.

Starting from the (shifted) Dirac equation (2.45), an expression for the small component can be extracted from the lower equation.

$$\psi^S = \left(1 + \frac{E - V}{2mc^2}\right)^{-1} \frac{\boldsymbol{\sigma} \cdot \mathbf{p}}{2mc} \psi^L = K \frac{\boldsymbol{\sigma} \cdot \mathbf{p}}{2mc} \psi^L, \quad (2.52)$$

which is very similar to the expression of the restricted kinetic balance (2.49), apart from the local multiplicative factor K . Substitution of ψ^S in the upper equation of (2.45), yields

$$\left\{ \frac{1}{2m} (\boldsymbol{\sigma} \cdot \mathbf{p}) K (\boldsymbol{\sigma} \cdot \mathbf{p}) + V \right\} \psi^L = E \psi^L. \quad (2.53)$$

This equation is known as the Unnormalized Elimination of the Small Component (UESC) equation. Because the large component wave function is not normalized, an extra normalization factor needs to be included in the wave function.

$$\psi = N \psi^L \quad (2.54)$$

$$N = \sqrt{1 + \frac{1}{4m^2 c^2} (\boldsymbol{\sigma} \cdot \mathbf{p}) K^2 (\boldsymbol{\sigma} \cdot \mathbf{p})} \quad (2.55)$$

The UESC equation is not a proper eigenvalue equation, since the factor K includes the energy E . We can however make approximations to K . For small values of E and V , it can be expanded in a series with $(E - V)/2mc^2$ as the expansion variable. The zeroth order term gives the non-relativistic Schrödinger equation. The first order terms give the relativistic corrections: the Darwin, mass-velocity and spin-orbit coupling operators.

In the case of a point charge nucleus, the potential $V \sim r^{-1}$ becomes infinite at the nucleus and the approximation will break down. It is however possible to write K as

$$K = \left(1 + \frac{E - V}{2mc^2}\right)^{-1} = \left(1 - \frac{V}{2mc^2}\right)^{-1} \left(1 + \frac{E}{2mc^2 - V}\right)^{-1} \quad (2.56)$$

and use $E/(2mc^2 - V)$ as the expansion parameter. Since the energy E is constant and always much smaller than $2mc^2 - V$, this Regular Approximation (RA)

is applicable everywhere, in particular near point nuclei. In calculations of valence properties, the zeroth order approximation (ZORA) is often used,

$$\left\{ \frac{1}{2m} (\boldsymbol{\sigma} \cdot \mathbf{p}) \left(1 - \frac{V}{2mc^2} \right)^{-1} (\boldsymbol{\sigma} \cdot \mathbf{p}) + V \right\} \psi^{\text{ZORA}} = E \psi^{\text{ZORA}}. \quad (2.57)$$

This is a proper eigenvalue equation with a Hamiltonian that is universal for all eigenstates, in contrast to the UESC equation (2.53).

For core properties, the ZORA approach is too approximate. A major problem with higher order regular approximations, or using UESC directly, is the dependence of the Hamiltonian on the energy, making the formalism state-specific. We can however perform a similar elimination of the small component, starting from the matrix form of the Dirac equation (2.50) and expressing the coefficient matrix of the small component in terms of that of the large component times a transformation matrix \mathbf{U} .

$$\mathbf{B} = \mathbf{U} \mathbf{A} \quad (2.58)$$

We can extract an expression for \mathbf{U} from the upper equation of (2.50), contrary to the UESC method, which uses the lower equation,

$$\mathbf{U} = \mathbf{T}^{-1} [\mathbf{S} \mathbf{A} \mathbf{E} \mathbf{A}^{-1} - \mathbf{V}]. \quad (2.59)$$

When we substitute for \mathbf{B} (2.58) into (2.50), premultiply the lower equation with \mathbf{U}^\dagger and add it to the upper equation, we get

$$\left[\underbrace{\mathbf{T} \mathbf{U} + \mathbf{U}^\dagger \mathbf{T} - \mathbf{U}^\dagger \mathbf{T} \mathbf{U}}_{\tilde{\mathbf{T}}} + \underbrace{\mathbf{V} + \mathbf{U}^\dagger \mathbf{W} \mathbf{U}}_{\tilde{\mathbf{V}}} \right] \mathbf{A} = \left[\underbrace{\mathbf{S} + \frac{1}{2mc^2} \mathbf{U}^\dagger \mathbf{T} \mathbf{U}}_{\tilde{\mathbf{S}}} \right] \mathbf{A} \mathbf{E} \quad (2.60)$$

$$\tilde{\mathbf{L}} \mathbf{A} = \tilde{\mathbf{S}} \mathbf{A} \mathbf{E}. \quad (2.61)$$

This equation looks similar to the Schrödinger equation, but with a modified Hamiltonian $\tilde{\mathbf{L}}$, consisting of the modified kinetic energy $\tilde{\mathbf{T}}$ and potential energy $\tilde{\mathbf{V}}$, and a modified metric $\tilde{\mathbf{S}}$. It is constructed such that if the large component wave function is normalized on the modified metric (= relativistic metric), the original four-

component wave function is also normalized.

$$\mathbf{A}^\dagger \tilde{\mathbf{S}} \mathbf{A} = \mathbf{A}^\dagger \mathbf{S} \mathbf{A} + \frac{1}{2mc^2} \mathbf{A}^\dagger \mathbf{U}^\dagger \mathbf{T} \mathbf{U} \mathbf{A} = \mathbf{A}^\dagger \mathbf{S} \mathbf{A} + \frac{1}{2mc^2} \mathbf{B}^\dagger \mathbf{T} \mathbf{B} = 1 \quad (2.62)$$

Therefore, Eq. (2.60) has been termed the Normalized Elimination of the Small Component (NESC).

It must be noted that NESC is not the only way to perform the reduction from a four-component to a two-component formalism. Some other two-component approaches are, amongst others, the Douglas–Kroll–Hess (DKH) method [65, 66, 67], the X2C theory [68], an implementation formulated by Iliáš and Saue [69, 70] and the infinite-order two-component (IOTC) method formulated by Barysz and Sadley [71, 72, 73, 53].

The transformation from four-component to two-component form is useful to reduce the computational effort. Care must however be taken in the calculation of observables, i.e. the expectation values of hermitian operators. In the four-component Dirac picture, the expectation value of the 4×4 operator \hat{X} is

$$\langle \hat{X} \rangle = \langle \Psi | \hat{X} | \Psi \rangle. \quad (2.63)$$

To get the expression in terms of the two-component NESC wave function, it helps to picture the NESC wave function as the result of some unitary transformation of the four-component wave function, such that the small component vanishes:

$$\hat{U} \Psi = \tilde{\Psi} = \begin{pmatrix} \tilde{\psi}^L \\ 0 \end{pmatrix} \quad (2.64)$$

The expectation value in the two-component picture is then

$$\begin{aligned} \langle \hat{X} \rangle &= \langle \Psi | \hat{U}^\dagger \hat{U} \hat{X} \hat{U}^\dagger \hat{U} | \Psi \rangle \\ &= \langle \tilde{\Psi} | \hat{U} \hat{X} \hat{U}^\dagger | \tilde{\Psi} \rangle \\ &= \langle \tilde{\psi}^L | \tilde{X}^{LL} | \tilde{\psi}^L \rangle, \end{aligned} \quad (2.65)$$

with \tilde{X}^{LL} the top-left 2×2 block of the operator $\hat{U} \hat{X} \hat{U}^\dagger$. This means that the expectation values of these operators can be calculated from the two-component wave function, as long as we also transform the operator using the same unitary trans-

formation. This is however not very practical in general, and the untransformed operator is used instead. Neglecting the transformation of these operators leads to the *picture change error* (PCE), which may be large for operators which assume large values in the vicinity of nuclei [74]. Since we are not calculating deep core properties of very heavy nuclei, the PCE may safely be ignored for the present work.

2.2.3 Implementation of the Normalized Elimination of the Small Component

In order to calculate the transformation matrix \mathbf{U} , we start from a suitable starting guess based on the same approximation as ZORA (2.57), effectively neglecting the energy-dependent term in Eq. (2.59),

$$\mathbf{U}_0 = (\mathbf{T} - \mathbf{W})^{-1} \mathbf{T} \quad (2.66)$$

When we substitute this expression for \mathbf{U} in the NESC equation (2.60), we end up with a formalism that is zeroth-order in the transformation matrix, but uses the exact (“infinite-order”) relativistic metric. This is contrary to the ZORA formalism, which uses the non-relativistic metric. Therefore this method has been termed the Infinite Order Regular Approximation (IORA).

The IORA approximation can be used as a starting guess for an iterative scheme to calculate the exact \mathbf{U} . After substitution of \mathbf{U}_0 into Eq. (2.60), we can diagonalize it to obtain the diagonal energy matrix \mathbf{E} , containing the energies of all states expressible within the basis set. Then we substitute \mathbf{E} into Eq. (2.59) to obtain the next guess for \mathbf{U} . This procedure is repeated until convergence has been reached, i.e. the energies and transformation matrix do not change within some threshold. In this way, a transformation matrix is constructed which is suitable for all eigenstates, rather than a state-specific one.

It has been shown by Filatov and Dyll [75] that this scheme is not guaranteed to converge. Convergence is especially difficult when tight basis functions are present, since these are not well suited to describe the weak singularity of the wave function near a point nucleus. A major problem is that in a limited basis IORA states of energies $> 2mc^2$ arise, which are very artificial in nature. Therefore it has been suggested to remove these erroneous solutions from the spectrum, using a fuzzy cutoff condition. In order to do so, the defining equation of \mathbf{U} (2.59)

has to be rewritten somewhat,

$$\mathbf{U} = \mathbf{T}^{-1} \left[\mathbf{S} \mathbf{A} \mathbf{d} \mathbf{A}^\dagger \tilde{\mathbf{L}} - \mathbf{V} \right]. \quad (2.67)$$

Here, the diagonal matrix \mathbf{d} has been introduced, which filters the states included in the optimization of \mathbf{U} . Diagonal element d_k is the weight of state k and is dependent on the energy of that state E_k in the following way,

$$d_k = \begin{cases} 1 & E_k \leq 0 \\ \left(1 + \frac{E_k}{2mc^2}\right)^{-1} & E_k > 0 \end{cases}. \quad (2.68)$$

This way all bound states are included in the optimization with the same weights as before, while the unbound states get smaller weights the higher their energies are.

The formalism described above provides the exact electronic solutions of the four-component one-electron problem. To be able to use this solution and the pertinent Hamiltonian operator $\tilde{\mathbf{L}}$ (2.60) for the calculation of a many-electron system using a standard non-relativistic quantum chemical code one can employ the one-electron approximation [55] within which the NESC one-electron Hamiltonian renormalized on the non-relativistic metric

$$\mathbf{H}_{1-e} = \mathbf{S}^{1/2} \tilde{\mathbf{S}}^{-1/2} \tilde{\mathbf{L}} \tilde{\mathbf{S}}^{-1/2} \mathbf{S}^{1/2} \quad (2.69)$$

is used in connection with the non-relativistic many-electron equations. We choose to take the scalar form of NESC (i.e. \mathbf{W} is the matrix representation of $(4m^2c^2)^{-1} \times \mathbf{p}V\mathbf{p}$). The transformation matrix \mathbf{U} is optimized using the bare nuclear potential, plus possibly the external potential. After optimization, this one-electron Hamiltonian is used in place of the non-relativistic one-electron Hamiltonian in a Hartree-Fock or RASSCF calculation, thereby incorporating the most important scalar-relativistic effects. It however means that the same \mathbf{U} is used for the one-electron system as for the many-electron system, which is a slight approximation. A more accurate approach would be to re-optimize \mathbf{U} in every iteration of the many-electron program. This is however computationally much more demanding and we choose to use the one-electron \mathbf{U} .

The incorporation of spin-orbit effect is done via the Spin-Orbit RAS State Interaction method (SO-RASSI). The method's approach is to add the spin-orbit operator to the Hamiltonian and diagonalize the resulting matrix in the basis of

RASSCF wave functions, with elements

$$H_{ij} = \langle \Psi_i | \hat{H}^{\text{SF}} + \hat{H}^{\text{SO}} | \Psi_j \rangle. \quad (2.70)$$

Here \hat{H}^{SF} is the spin-free Hamiltonian, as was used in the preceding RASSCF calculation. If the RASSCF states are all from a single (state averaged) RASSCF calculation, the interaction comes purely from the spin-orbit interaction \hat{H}^{SO} .

From the Dirac-Coulomb-Breit Hamiltonian (2.46), the spin-orbit part can be extracted, which has the following form:

$$\begin{aligned} \hat{H}^{\text{SO}} &= \frac{1}{2m^2c^2} \left[\sum_{i\mu} Z_\mu \frac{\mathbf{l}_{i\mu} \mathbf{s}_i}{r_{i\mu}^3} - \sum_{i \neq j} \frac{\mathbf{l}_{ij} (\mathbf{s}_i + 2\mathbf{s}_j)}{r_{ij}^3} \right] \\ &= \sum_i \hat{H}^{\text{SO}}(i) + \sum_{ij} \hat{H}^{\text{SO}}(i, j) \end{aligned} \quad (2.71)$$

Especially the second (two-electron) term is very hard to compute, therefore we make an approximation by transforming to an effective one-electron form. The matrix element of this operator between Slater determinants which differ by a single excitation $i \rightarrow j$ is then

$$\begin{aligned} H_{ij}^{\text{SO}} &= \langle i | \hat{H}^{\text{SO}}(1) | j \rangle + \frac{1}{2} \sum_k n_k \left[\langle ik | \hat{H}^{\text{SO}}(1, 2) | jk \rangle - \right. \\ &\quad \left. \langle ik | \hat{H}^{\text{SO}}(1, 2) | kj \rangle - \langle ki | \hat{H}^{\text{SO}}(1, 2) | jk \rangle \right] \end{aligned} \quad (2.72)$$

The mean field approximation is included by setting the occupation numbers n_k equal to the *average* occupation number of spin-orbital k . To reduce the computational effort even further also the one-center approximation is included, which means that only integrals from basis functions which all belong to same atom are included (the Atomic Mean Field Integrals (AMFI)) [57] (see also [76]). Using these two approximations reduces the time needed for the SOC evaluation to a negligible amount.

The default implementation of AMFI in Molcas [56] assumes that the atomic orbitals used for the atomic mean field are the first basis functions in the basis set. This is a valid assumption when using the atomic natural orbital (ANO) type basis sets, which are included as the default basis sets in Molcas. However, when

using an uncontracted basis set, as we did in most of our calculations, the default implementation gives wildly inaccurate spin-orbit splittings. Therefore, we have used a modified implementation of AMFI [77] (see also [78]), which performs a relativistic atomic ground state calculation to yield the orbital coefficients to use in the mean field definition.

2.3 The embedded cluster model

Calculations on crystalline solid state systems consisting of an enormous number of atoms are computationally impossible with the methods described so far. There are various options to describe this kind of systems. One is to model the system by an infinite array of atoms and make use of the translational symmetry, leading to the well-known band theory. A second option is to model the system by describing only a small part of the system (the cluster) by quantum-chemical methods and the rest by a more approximate level of theory. The latter is preferable, because the effects of relaxation and correlation, which are very important for the description of core-ionizations and -excitations, can be easily included in the calculation. These localized effects are very hard to describe well in band theory.

For ionic crystals, the simplest approximation to describe the remainder of the crystal in the embedded cluster model is by replacing the crystal atoms outside the cluster by point charges q_j equal to the corresponding formal charges. The static Madelung potential generated by these charges,

$$V'_M(\mathbf{r}) = \sum_{j \in \text{PC}} \frac{q_j}{|\mathbf{r}_j - \mathbf{r}|}, \quad (2.73)$$

is then added to the one-electron part of the cluster Hamiltonian. The prime in V'_M indicates that those point charges which belong to cluster atoms have been removed from the sum. The (infinite) sum over point charges is in general conditionally convergent and care should be taken in which order the terms are summed to get a convergent sum. Depending on the choice of unit cell, there may be an arbitrary shift of the Madelung potential over the cluster, which is however constant over the cluster and therefore physically insignificant. For finite sample sizes, the Madelung potential is also dependent on the dipole moment, as well as the shape of the sample [79].

In practice, the infinite sum over point charges is usually replaced by a sum

over a limited number of point charges, which have been adapted to yield the same Madelung potential in the cluster region as the infinite sum. This adaptation can be done by fitting the charges to give the correct Madelung potential. For sufficiently simple crystal structures, a more straightforward way to adapt the point charges is by Evjen's scheme [80]. In this scheme the point charges are limited to a supercell composed of a fixed number of unit cells extending in each direction. At the edges of this supercell, the charges are scaled down by a factor depending on the position. For example for a cubic lattice, at the face of the supercell this factor is 1/2, at the edge it is 1/4 and at a vertex it is 1/8.

2.3.1 *Ab initio* embedding model potentials

Modeling the crystal environment by point charges is very crude since it does not take the shape of the electronic cloud around the surrounding atoms into account. Also, the charges produce a classical Coulomb potential and quantum effects (most notably the exchange interaction) are completely ignored. A better approximation is to replace the point charges representing the embedding ions in the near vicinity of the cluster by *Ab Initio* Model Potentials (AIMP's). The Hamiltonian of the embedded cluster can then be written as

$$\hat{H}_{\text{embedded cluster}} = \hat{H}_{\text{isolated cluster}} + \sum_i^{\text{cluster electrons}} \left[\sum_{\xi}^{\text{embedding ions}} \hat{V}_{\xi}^{\text{AIMP}}(i) + V_M''(i) \right], \quad (2.74)$$

where the double prime in V_M'' indicates that the nearest point charges, which are now included in the sum over AIMP's, have been removed from the Madelung potential. The AIMP of embedding ion ξ is given by

$$\hat{V}_{\xi}^{\text{AIMP}}(i) = -\frac{q_{\xi}}{r_{\xi i}} + \frac{1}{r_{\xi i}} \sum_p C_p^{\xi} \exp(-\alpha_p^{\xi} r_{\xi i}^2) + \sum_p \sum_q |\chi_p^{\xi}\rangle A_{pq}^{\xi} \langle \chi_q^{\xi}| + \sum_k B_k^{\xi} |\psi_k^{\xi}\rangle \langle \psi_k^{\xi}|. \quad (2.75)$$

The first term is again the potential of a point charge with the formal charge q_{ξ} of the embedding ion. The second term is a correction to the point charge that takes into account the Coulomb potential of the electronic cloud, with sets of parameters

C_p^ξ and α_p^ξ fitted such that

$$\frac{1}{r_{\xi i}} \sum_p C_p^\xi \exp(-\alpha_p^\xi r_{\xi i}^2) \approx -\frac{N_\xi^e}{r_{\xi i}} + 2 \sum_k f_k \int \frac{\psi_k^{\xi*}(j) \psi_k^\xi(j)}{r_{ij}} d\tau_j, \quad (2.76)$$

with f_k the fractional occupation number of the atomic orbital ψ_k^ξ of ion ξ . The third term in Eq. (2.75) describes the exchange interaction between the cluster electrons and the embedding electrons, in terms of a set of auxiliary basis functions χ^ξ chosen to represent the orbitals of the embedding ion ξ . It has the form of a spectral representation with

$$A_{pq}^\xi = - \sum_r \sum_s S_{pr}^{-1} \sum_k n_k \int \frac{\chi_r^{\xi*}(i) \psi_k^{\xi*}(j) \psi_k^\xi(i) \chi_s^\xi(j)}{r_{ij}} d\tau_i d\tau_j S_{sq}^{-1}, \quad (2.77)$$

with the overlap matrix $S_{pq} = \langle \chi_p^\xi | \chi_q^\xi \rangle$.

The last term is the frozen-orbital shifting operator, which prevents the cluster electrons to occupy orbitals on the embedding ions, thereby ensuring that the Pauli principle is obeyed. The value of B_k has long been the subject of debate. The first derivation [81] of $B_k = -\epsilon_k$ was later corrected [82] to $B_k = -2\epsilon_k$. It has been shown by Pascual et al. [83] however that this value should be tuned when optimizing the potential. The reason is the arbitrary shift in the electrostatic potential, as discussed above, which may lead to a different set of orbital energies and therefore different values for B_k . Problems also occur if occupied orbitals with positive orbital energies are present, since this will lead to a negative B_k and therefore *enforce* cluster electrons to occupy these embedding ion orbitals. The tuning procedure is however quite demanding and, moreover, for our systems these problems are not expected to occur, hence we stick to the “traditional” choice of $B_k = -2\epsilon_k$.

All parameters are optimized in a self-consistent embedded ions (SCEI) calculation. In this procedure, the AIMP’s of all elements present in the crystal are optimized simultaneously. The first step is to calculate for each element the (SCF, RASSCF) wave function of a single ion in the field of formal point charges describing the crystal. For each of these elements, the AIMP is calculated by fitting of Eq. (2.76) and calculating the other necessary parameters. Then the point charges are replaced by these AIMP’s and the procedure is repeated until the potentials do not change significantly anymore. The auxiliary basis set $\{\chi^\xi\}$ is optimized simultaneously, but an optimization step is only performed every couple of iterations.

2.3.2 Extra-cluster relaxation

Upon a core excitation or ionization, the electronic density of the cluster may change considerably and this induces a response in the remainder of the crystal. The primary effect is the electronic response of the surroundings, which can finally lead to a structural effect: the formation of a polaron. In the embedded cluster model discussed so far, the embedding potential remains static after optimization for the ground state of the system. It is therefore unable to describe this extra-cluster relaxation.

Extra-cluster relaxation may be included by applying the discrete reaction field (DRF) method, preferably in the self-consistent form [84]. In this method, an extra term describing the induced dipole is added to the AIMP's of the embedding ions. After the calculation with the static embedding, the induced dipoles are calculated from tabulated values of the atomic polarizability. In this way a new embedding potential is generated and again this procedure may be repeated until the energy of the cluster state of interest does not change anymore.

For our XPS calculations, the inclusion of these effects is important, since the introduction of the extra +1 charge gives rise to a large response in the surroundings. We do however expect that the accompanied shift in energy is more or less constant for all final states. It will therefore give rise to a rigid shift of the calculated spectrum as compared to the experimental spectrum. Since we already choose to shift the spectrum rigidly to match the experimental spectrum, we can safely ignore the extra-cluster relaxation effects in our calculations. Also, in those calculations where a comparison is made to accurate four-component calculations, the systems described should be the same, i.e. in most cases a single atom without any embedding.

In the case of XAS, the extra-cluster relaxation effects are less pronounced, since the charge of the cluster does not change upon excitation. In our XAS calculations, a comparison is made to experimental results on small clusters which are small enough to be modeled without the embedded cluster approximation.

Chapter 3

Theoretical Core Spectroscopy

Core spectroscopies like X-ray photoelectron spectroscopy (XPS) and X-ray absorption spectroscopy (XAS) are powerful techniques to study the electronic structure of matter. In XPS, an electron from a core shell is ionized by X-rays of known energy and the kinetic energy of the electron is measured. The binding energy of that electron is the difference of these energies. In XAS, the electron is excited to the valence shell instead, and the absorption of the X-rays is measured. The electron binding energies and the absorption energies, along with their relative intensities, can give very detailed information on the electronic structure of the system of interest. However, the interpretation of the resulting spectra is often not straightforward, especially when systems containing open shell atoms or ions are studied. In order to reproduce experimental spectra from theory, two quantities should be calculated: the binding (XPS) or excitation (XAS) energies of the electron(s) of interest and the transition probability.

A computational spectrum generated from energies and transition probabilities consists of a collection of lines, whereas an experimental spectrum contains peaks with a certain width. One aspect that needs to be pointed at is line broadening. Broadenings occur due to experimental conditions, such as the energy distribution of the incoming photons, charging of the sample, and, for XPS, the resolution of the energy of the outgoing electrons. The broadening due to the first effect may range from 0.25 eV to 1 eV full width at half maximum (FWHM) [85, 86, 87]. In addition, peaks may be broadened by inhomogeneous materials. An intrinsic cause for broadening is the lifetime of the core-hole state [10]. Finally, vibrational or Frank-Condon broadening [88], due to the vibrational motion, is important [89]. Although vibrational broadening can be included from first principles in computational spectra, these broadenings are often introduced a posteriori, via a Lorentzian and/or Gaussian curve.

3.1 Binding and excitation energies

The binding energy of an electron can be determined according to Koopmans' theorem from the orbital energy of that electron in a restricted Hartree-Fock (RHF) calculation. This 'Frozen Orbital' approach gives quite accurate results for the first ionization energy of many closed-shell systems. This is however due to the fortunate cancellation of two effects which are not taken into account by this approximation. First, it is assumed that the orbitals do not change upon ionization. Neglecting this orbital relaxation leads to an overestimation of the ionization energy. The second effect is that the RHF method does not include electron correlation. Electron correlation always leads to an energy lowering, which depends on the number of electrons in the system. In fact, the energy lowering is generally greater for the N -electron system than for the $(N-1)$ -electron system. It can be concluded that neglecting electron correlation usually leads to an underestimation of the ionization energy.

In the case of ionization of valence electrons, the relaxation energy in the final state and the difference of correlation energies of initial and final state are of comparable magnitude. For core electrons this is not the case. The spatial extent of the core orbitals is very small compared to the valence orbitals. When an electron is removed from one of these core orbitals, the potential changes drastically. In many cases it is even comparable to the change induced by increasing the nuclear charge with $+1$.¹ The remaining electrons are more attracted by the higher effective nuclear charge, screening the core hole, leading to a higher relaxation energy than in the case of ionization of valence electrons. Therefore Koopmans' theorem gives a too high estimate of the binding energy.

The major problem with Koopmans' theorem is that it only takes initial state effects into account. Final state effects, like orbital relaxation, charge transfer and angular momentum coupling are completely neglected. Applying the frozen orbital approach to compute excitation energies leads to similar problems. A more accurate way to calculate binding energies and excitation energies is by using the so-called Δ SCF procedure. This is done by performing calculations on the initial state and the final (ionized or excited) state separately, after which the binding/excitation energy can be determined as the difference in total energies. Since

¹The equivalent core approximation [90] is based on this notion: the binding energy of a core electron may be found by approximating the wave function of the core-ionized atom with nuclear charge Z , i.e. $[Z]^{*+}$, by the ground state wave function of $[Z + 1]^+$.

we cannot depend on the fortunate cancellation of the correlation energy, we need to take correlation effects into account explicitly using one of the methods as described in Chapter 2.

3.2 Angular momentum coupling

An important final state effect is angular momentum coupling. The interpretation of angular momentum coupling in atoms is usually done in one of two schemes: Russell-Saunders (LS) coupling and j-j coupling.

In Russell-Saunders coupling, the orbital momenta l of all electrons are first coupled to a total L . For 2 electrons, the total L can have values

$$L = |l_1 - l_2|, |l_1 - l_2| + 1, \dots, l_1 + l_2. \quad (3.1)$$

More electrons can be coupled by repeatedly applying this rule. Using the same rule, the spin momenta s of all electrons couple to a total S and the total orbital momentum L and total spin momentum S couple to the total angular momentum J . An electronic state with orbital, spin and total angular momenta L , S and J is then denoted by its term symbol, $^{2S+1}\{L\}_J$, where $2S + 1$ is the spin multiplicity of the state.

In the j-j coupling scheme, the orbital and spin momentum is first coupled to a total momentum j for each electron separately

$$j = |l - s|, |l - s| + 1, \dots, l + s, \quad (3.2)$$

after which the momenta of all electrons couple to the total angular momentum J . Both the LS and j-j coupling schemes are equally correct in the sense that they give the same set of states as defined by their J-values. However, the grouping into multiplets is different, and the choice of coupling scheme and its usefulness in the interpretation of a core spectrum depends on the system of interest.

The applicability of a certain coupling scheme depends on the strength of spin-orbit coupling. In the valence shell of light elements, where spin-orbit coupling is weak, the RS coupling scheme gives the best insight. In case of strong spin-orbit coupling, i.e. in the valence shell of heavy elements and the core shells of almost all elements, the j-j coupling scheme is more insightful.

Insight in the spin-orbit and angular momentum coupling of the final states is

very useful for the interpretation of core spectra. The main peaks in XPS spectra can be assigned by looking at the total angular momentum before ionization, and couple the angular momentum of the introduced core-hole to it. For example, the 1s XPS of the open-shell K atom shows 2 peaks, coming from the coupling of the 1s hole ($l = 0, s = 1/2$) to the ground state $^2S_{1/2}$, leading to a 1S_0 and a 3S_1 final state, respectively. If a core-hole with $l \geq 1$ is introduced, the spectrum is usually dominated by the spin-orbit coupling in the core shell. This will give rise to two main structures in the spectrum, coming from the coupling of either the $j = l - 1/2$ or the $j = l + 1/2$ core-hole to the initial state. For example, the 2p XPS of the K atom shows in principle four peaks. Two peaks are originating from the coupling of the $2p_{1/2}$ hole to the initial state $^2S_{1/2}$, leading to $J = 0$ and $J = 1$ states. Two more peaks originate from the coupling of the $2p_{3/2}$ hole to the initial state, leading to $J = 1$ and $J = 2$ states. The energy splitting due to this exchange coupling is however much smaller than the spin-orbit coupling in the 2p shell, and these peaks may not be resolved in an experimental spectrum. For similar systems where the spin-orbit coupling is weak in the initial state but strong in the final states due to the introduction of a ($l \geq 1$) core-hole, this mixed coupling scheme is insightful.

Relativistic ab-initio calculations are able to treat the whole range between weak and strong spin-orbit coupling, and those results are often said to be obtained in intermediate coupling.

3.3 Transition probabilities

During the core excitation or ionization, the total angular momentum should be conserved. The selection rules describing the possible transitions are based on the fact that the photon itself has an angular momentum of 1. The computed transition probabilities considered in this thesis are based on the dipole approximation while electric quadrupole and magnetic dipole contributions are ignored. The question of validity of the dipole approximation for core p electron excitations has been addressed in a number of recent publications. Saldin and Ueda [91] discussed the validity of the dipole approximation in electron energy loss spectroscopy due to L-shell excitations for chemical elements with Z up to 50. They found that the dipole approximation is likely to be good for primary energies of the order of 100 keV for all the L edges of all elements studied. Nuroh [92] validated

the conclusions arrived at by Saldin and Ueda that dipole transitions are the most significant contributions in L-shell electron excitation spectra.

The possible contribution of quadrupolar contributions to metal K-edge absorption spectrum has been discussed for transition metal oxides metal [93]. For TiO_2 and V_2O_5 the interpretation of experimental spectra revealed a contribution of quadrupole transitions to the pre-edge structures, although these are dominated by dipole transitions [94, 95, 96]. Of course, non-dipole transitions may become important when there are many dipole-forbidden states in energy regions where there are no dipole allowed transitions, but we will ignore these effects in the present work.

For excitations, the relative intensity in the dipole approximation of the transition of initial state Ψ^I to final state Ψ^F is proportional to the oscillator strength between those states,

$$I_{F \leftarrow I}^{\text{rel}} \propto \frac{2}{3} (E_F - E_I) |\langle \Psi^I | \mathbf{r} | \Psi^F \rangle|^2. \quad (3.3)$$

From symmetry arguments, it can be seen that in the absence of spin-orbit coupling the probability is zero unless the transition changes the orbital angular momentum by $\Delta L = \pm 1$, while the spin angular momentum does not change ($\Delta S = 0$). In the presence of spin-orbit coupling, the only excitations which are allowed are those which change the total angular momentum by $\Delta J = \pm 1$. For simple systems, the ratio of transition intensities is equal to the statistical ratio of the states of interest. However, due to the angular momentum coupling in the valence shell, external crystal and covalent effects these ratios may strongly deviate from the statistical values.

In the case of core-ionization, the transition intensities can be found using the sudden approximation (SA) [58]. In the sudden approximation, it is assumed that the ionization from the core orbital and the associated change in Coulombic field happens instantaneously, an assumption which is only valid when the energy of the incident radiation is much greater than the binding energy of the emitted electron. Even though the ionization happens instantaneously, the time-dependent wave function must still be a continuous function in time, which leads to the formulation of the transition intensity. The relative intensity for the transition of initial state Ψ^I to final state Ψ^F through the ionization from core orbital r may be approximated as

$$I_{F \leftarrow I}^{\text{rel}}(r) \propto |\langle \hat{a}_r \Psi^I | \Psi^F \rangle|^2. \quad (3.4)$$

The effect of the annihilator \hat{a}_r is that it removes one electron from orbital r of the initial state. The physical interpretation is that at the moment of ionization the core electron is suddenly removed and the system is in a superposition of final states. Afterwards, the system can relax to one of the final states, with the probability dependent on its overlap with the "frozen" final state $\hat{a}_r\Psi^I$.

In the present work, the complete active space SCF (CASSCF) method is used for the calculation of the initial state Ψ^I of the target many-electron system. Because with the use of the Hamiltonian (2.69) only scalar relativistic effects are taken into account, the RASSI approach [56] combined with the AMFI method [57] is used to take the SO effects into account. The wave function Ψ^I of the initial state of the system is then given by a linear combination of the spin-free states² as in Eq. (3.5),

$$\Psi_i^I = \sum_S \sum_{M_S=-S}^S \sum_j C_{ij}^{\text{SO}}(S, M_S) \sum_k C_{jk}^{\text{CI}} \Phi_k(S, M_S) \quad (3.5)$$

where C_{ij}^{SO} are the expansion coefficients of the spin-orbit coupled state Ψ_i^I in terms of spin-free CASSCF wave functions. The latter wave functions are expanded in terms of the configuration state functions (CSFs) $\Phi_k(S, M_S)$ with the CI coefficients C_{jk}^{CI} obtained in the CASSCF calculation.

The final states Ψ^F of the ionized system are calculated with the use of the restricted active space SCF (RASSCF) formalism whereby the core orbitals from which the ionization occurs are restricted to accommodate at least (or at most) one hole and the SO interaction is treated using the RASSI/AMFI approach. Equivalent to the initial state wave function Ψ^I , the final state wave function Ψ^F is expanded in terms of the spin-free CSFs as

$$\Psi_n^F = \sum_{S'} \sum_{M_{S'}=-S'}^{S'} \sum_m C_{nm}^{\text{SO}}(S', M_{S'}) \sum_l C_{ml}^{\text{CI}} \Phi_l(S', M_{S'}) \quad (3.6)$$

where the summation with respect to the spin S' runs over an extended range of values due to the coupling of the spin of the hole with the spin of the valence shell in the spin-free CSFs $\Phi_l(S', M_{S'})$.

²Note that by "spin-free states" we mean eigenstates of the spin-free Hamiltonian, i.e. without taking spin-orbit coupling into account. These states *do* have a spin associated with them, as given by the quantum numbers S and M_S .

It can be seen that states of different spin symmetry (S, M_S) can mix under the influence of the spin-orbit Hamiltonian. For the initial state only those CASSCF CSFs are included in the expansion that are expected to have a reasonable contribution to the single initial state. After ionization, there are however a lot of possible final states and the RASSCF CSF's included in the expansion should be able to describe all those final states.

Only the CSFs are affected by the annihilation operator in the frozen final state (FFS) $\hat{a}\Psi^I$, the SO and CI coefficients are left unchanged. The orbitals used to construct the FFS $\hat{a}\Psi^I$ are identical to the orbitals of the initial state Ψ^I .

$$\hat{a}\Psi_i^I = \sum_S \sum_{M_S=-S}^S \sum_j C_{ij}^{\text{SO}}(S, M_S) \sum_k C_{jk}^{\text{CI}} \{ \hat{a}\Phi_k(S, M_S) \} \quad (3.7)$$

Annihilation of one electron in the initial state introduces an extra spin-1/2 in the core orbital which can be coupled in two different ways with the open shell valence electrons. Given that a CSF in the expansion of the initial state Ψ^I , Eq. (3.5) has total spin S , the CSFs with the total spin $S + 1/2$ and $S - 1/2$ emerge in the FFS. The contributions of the new CSFs into the FFS wave function can be derived using the "genealogical" construction [97], i.e. by successive coupling of the individual spins in the open shell orbitals with the spin in the ionized orbital. When deriving the FFS expansion in terms of CSFs, Eq. (3.8), both directions of the extra spin in the ionized orbitals, α and β , were taken with equal weights.

$$\begin{aligned} \hat{a}\Psi_i^I = & \sum_S \sum_{M_S=-S}^S \sum_j C_{ij}^{\text{SO}}(S, M_S) \sum_k C_{jk}^{\text{CI}} \times \\ & \left\{ \sqrt{\frac{S+M_S+1}{4S+2}} \Phi_k(S+1/2, M_S+1/2) \right. \\ & + \sqrt{\frac{S-M_S+1}{4S+2}} \Phi_k(S+1/2, M_S-1/2) \\ & - \sqrt{\frac{S-M_S}{4S+2}} \Phi_k(S-1/2, M_S+1/2) \\ & \left. + \sqrt{\frac{S+M_S}{4S+2}} \Phi_k(S-1/2, M_S-1/2) \right\} \quad (3.8) \end{aligned}$$

Eq. (3.8) yields the expansion of the FFS in terms of the CSFs with the same to-

tal spin S and projection of the spin M_S as appear in the expansion of the final state Ψ^F , Eq. (3.6). Therefore the relative intensities of the XPS spectral lines can be calculated from the overlap integrals between the CSFs with the same spin symmetry and the CI and SO expansion coefficients in Eqs. (3.8) and (3.6).

In the construction of the FFS, it should be noted that the coupling is in the same order as the RAS spaces. Since the extra introduced spin is expected to couple lastly to the initial CSFs, the core orbital should be put in the RAS3 space. However, in the case of a single spin in RAS2 (i.e. an initial doublet state, $S = 1/2$) the coupling may be defined in the reverse order with the same coefficients (times -1 for $\Phi_k(0, 0)$, i.e. with a change of sign for the last two terms of Eq. 3.8). This allows the core orbital to be put in the RAS1 space, which is advantageous for those systems where putting the core orbitals in the RAS3 space would yield a too high number of CSFs. We use this approach, with the core orbitals in the RAS1 space, in the calculations of the XPS of uranium in Chapter 4.

3.4 The computational algorithms

The methods described here provide the toolbox to calculate from first principles the XAS and XPS spectra of many systems. We have used the Molcas 7.0 program and implemented the important missing modules, namely the NESC algorithm to take account of relativity and the Sudden Approximation for the transition intensities of XPS. In this section we describe the program flow for calculating the XAS and XPS of an open shell system.

The first step for both XAS and XPS is the calculation of the initial state wave function. We select those spin-free states which are expected to have a contribution to the spin-orbit coupled initial state wave function. These states are calculated by CASSCF, with the orbitals of the open valence shell put in the active space. The spin-free final states are calculated by RASSCF, with the valence shell orbitals in RAS2 and the selected core orbital(s) in RAS3 (or RAS1, as explained in section 2.1.3), allowing at most $2n_c - 1$ electrons in the RAS3 space. Using the SUPSYM keyword of the RASSCF module, the core orbitals are assigned a different symmetry group than the other orbitals. In this way, orbital rotations between the core orbitals of interest and the other orbitals are prevented and the wave function will have the expected core-hole even after orbital optimization.

For the XAS calculations, we do a single SO-RASSI calculation to compute spin-

orbit coupled states in the basis of both the spin-free initial states and the spin-free final states. In the RASSI module in Molcas, also the oscillator strength between all spin-orbit states is calculated. There will be an energy splitting in the initial state because of SOC, and we could describe the initial situation as a Boltzmann distribution over the lowest states. However, in the systems studied so far, the splitting was either very small so that the Boltzmann distribution (for any reasonable temperature) corresponds to a uniform distribution over all initial states, or very high such that only the lowest SO state was occupied.

For the XPS calculations, we do separate SO-RASSI calculations for the initial state and the final states. The binding energies are calculated as the difference of the initial state energy and the final state energies. For the computation of the transition intensities, we have developed two extra modules as part of the present project to be used in the Molcas calculations, namely SUDDEN and SO-OVERLAP.

The spin-free frozen final state is constructed using the module SUDDEN. In this module, the FFS CSF's are constructed by combining the orbitals of the initial state with the spin-structure of the final state CSF's, taking into account the mapping of IS CSF's to FS CSF's (Eq. 3.8). The order of the frozen final state CSF's is taken directly from the final state RASSCF calculation, so that it was not necessary to generate in our code the CSF's in the order expected by the other modules in Molcas. It is only necessary to locate, for every core orbital, the four matching CSF's in the set of CSF's generated for the final state. The FFS orbitals are then combined with the CI coefficients from the initial state CASSCF calculation to get the spin-free FFS.

The RASSI module is used again, be it now without the SO operator, to calculate the overlap between the spin-free frozen final states and the spin-free optimized final states. Finally, the overlap matrix is multiplied by the matrices of SO coefficients of the initial and final states (in the module SO-OVERLAP) to get the transition intensities for the SO states. The flow chart of the calculation of the XPS spectrum is depicted in Figure 3.1.

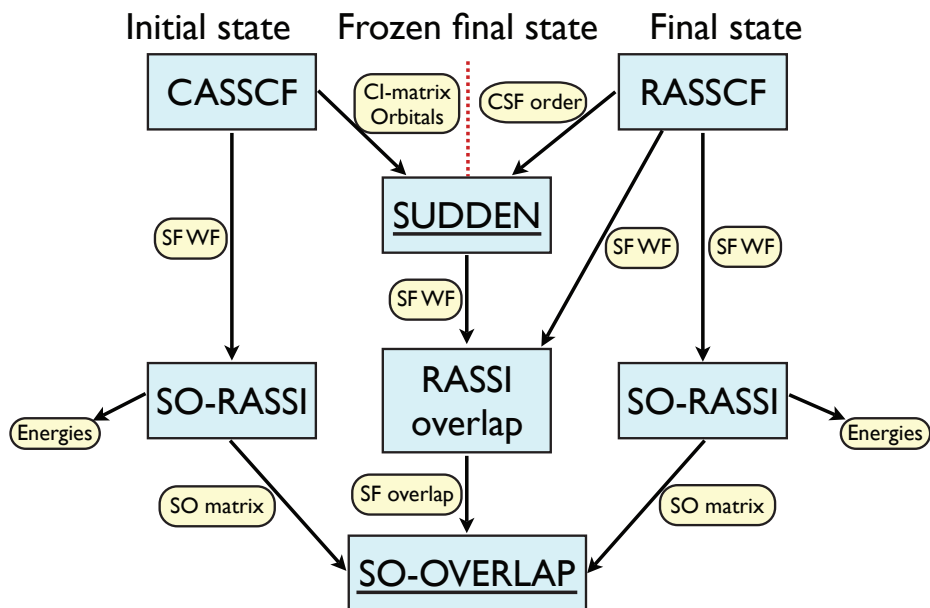


Figure 3.1: This diagram shows the data flow within a Molcas calculation of an XPS spectrum. The binding energies, calculated as the difference of final state and initial state energies, are available from the standard Molcas modules RASSCF and RASSI. The SUDDEN and SO-OVERLAP modules, which are essential for the calculation of the transition intensities, were developed as part of this work.

Chapter 4

Benchmark calculations on atomic uranium¹

In order to assess the quality of the developed formalism compared to the full four-component (4C) formalism, we calculate the 4f XPS spectrum of the uranium(V) ion. The 4f XPS of U^{5+} is interesting from a theoretical viewpoint, since, even for a qualitatively correct description of the initial and final states, it is essential to incorporate the effects of relativity and electronic correlation to a high degree. The initial ground state has a $[Rn] 5f^1$, which is split due to the relativistic effects of spin-orbit coupling. For the final states, a hole is introduced into the 4f shell, which is subject to an even stronger spin-orbit coupling compared to the 5f shell. The angular momentum of the introduced hole couples to that of the 5f electron, resulting in a number of final states of different energy.

The method described in the previous chapters is designed to take all these effects into account. In our computation of the 4f XPS of U^{5+} , the result is a spectrum with two main structures coming from the ionization of the two spin-orbit split 4f subshells. Each structure consists of several peaks from the various ways of angular momentum coupling of the hole to the valence electron.

Our results are compared to the accurate four-component results on the binding energies and relative intensities, which are available from the work of Bagus and Ilton [16, 17].

4.1 Details of calculations

The calculations employ the ANO-RCC-VQZP quadruple-zeta basis set with polarization functions [99]. The initial electronic configuration of U^{5+} is $[Rn] 5f^1$. This

¹Parts of this chapter have been published in R. Klooster, R. Broer and M. Filatov *Chem. Phys.* **2012**, 395 [98]

is described in the calculation by a state-averaged CASSCF calculation, with the single valence electron occupying the seven 5f orbitals in all possible ways. The orbitals are optimized to minimize the average energy of the seven possible doublet states. Spin-orbit interaction is included in the subsequent SO-RASSI in the basis of all CASSCF states, leading to two multiplets with $J = 5/2$ and $J = 7/2$.

The final states are constructed by distributing the valence electron in all possible ways over the 5f orbitals and the core hole in all possible ways over the 4f orbitals. This is done in the RASSCF calculations, where the 5f orbitals are put in the RAS2 space and the 4f orbitals in the RAS1 space, with a maximum of 1 hole, and a total of 14 active electrons. The 4f core orbitals are kept frozen in all calculations, whereas all other orbitals are either frozen or allowed to relax, corresponding to the two varieties of 4C calculations of Bagus and Ilton. Two state-averaged RASSCF calculations are done, one for the singlet states and one for the triplet states. In the singlet calculation, the lowest state does not include a core hole, and is given a weight close to zero². All final singlet and triplet RASSCF states with a single core hole are then used as a basis in the final state SO-RASSI calculation.

Note that this is an example where it is better to put the core orbitals in the RAS1 space instead of the RAS3 space. If we would put the 4f orbitals in the RAS3 space, we would need to allow up to 13-fold excitations from RAS2 to RAS3. This prevents the (single) configuration without the core hole from entering the calculation, but the configurations with a double, triple, etc. up to 13-tuple core holes are all included. The number of configurations ($\approx 10^7$), in combination with the reasonably large number of possible final states (≈ 50), is simply too high to allow the computation to be done. In contrast, the number of configurations in the performed calculations is equal to the number of states (50 and 49 for singlet and triplet, respectively).

Putting the core orbitals in the RAS1 space has an effect on the order of spin-coupling in the CSF's describing the frozen final state in the sudden approximation (Eq. 3.8). Because there is only one electron in the RAS2 space, this only involves a change of sign in the coefficients, as explained in section 3.3.

²Not exactly zero, since that would prevent the calculation to converge.

4.2 Results and discussion

The initial state of the U^{5+} ion has the single valence electron distributed over all 5f orbitals, which gives a 2F multiplet. When we include SO coupling, this multiplet splits into a ${}^2F_{5/2}$ ground state and a ${}^2F_{7/2}$ excited state separated by 1.0 eV. This splitting is large enough to assume that the system is completely in the ground state at room temperature.

The singlet state with lowest energy in the calculation corresponds to the ground state of closed shell U^{6+} (1S). The orbitals are optimized to minimize the average energy of all singlet states *except* this closed shell state. In the triplet case, all states are included in the orbital optimization. The 4f orbitals are kept frozen in both singlet and triplet calculations to prevent collapse to 5p-ionized states. The resulting Russel-Saunders terms are ${}^{1,3}S$, ${}^{1,3}P$, ${}^{1,3}D$, ${}^{1,3}F$, ${}^{1,3}G$, ${}^{1,3}H$ and ${}^{1,3}I$. Afterwards, the SO-split states are calculated in the same manner as for the initial state, yielding states of $J = 0, \dots, 7$.

The relative ionization intensities are calculated from the sudden approximation. The spin-free frozen final states are linear combinations of singlet and triplet states, with relative weights 1/4 and 3/4 respectively. If we would have considered SO coupling from the start, the initial state has a valence orbital occupation of $5f_{5/2}^1$ and the only XPS allowed final state configurations are $4f_{7/2}^{-1}5f_{5/2}^1$ and $4f_{5/2}^{-1}5f_{5/2}^1$. These can couple to a total $J = 1, 2, 3, 4, 5, 6$ for the first configuration, and $J = 0, 1, 2, 3, 4, 5$ for the second. In our calculation, also the configurations $4f_{7/2}^{-1}5f_{7/2}^1$ and $4f_{5/2}^{-1}5f_{7/2}^1$ are included, because in the spin-free calculation all 5f orbitals are equivalent. These configurations do not carry any intensity, but can still mix with the allowed configurations in the CI procedure, as long as the total J is the same as the XPS allowed configurations. This leads to “intensity stealing”, i.e. the states which have predominant $5f_{5/2}^1$ character will lose some intensity by mixing in $5f_{7/2}^1$ configurations, and the states which have predominant $5f_{7/2}^1$ character will gain some intensity by mixing in $5f_{5/2}^1$ configurations. The $J = 7$ level, which arises from the coupling of the $4f_{7/2}$ hole to the $5f_{7/2}$ electron (in LS terms, from 3I), is the only XPS forbidden level and hence has an intensity equal to zero. Indeed the contributions of the spin-free intensities to this SO level cancel.

For the final states, two types of calculations have been performed. In the first type, the orbitals of the final state were kept identical to the IS and only the CI coefficients were optimized. The results for the most important peaks are summarized in Table 4.1. In the second type, all orbitals, except the 4f orbitals from

J	$E_{\text{rel}}/\Delta E_{\text{rel}}(\text{eV})$	$E_{\text{rel}}^{4\text{C}}/\Delta E_{\text{rel}}^{4\text{C}}(\text{eV})$	I_{rel}	lost $I(\%)$	$I_{\text{rel}}^{4\text{C}}$	lost $I(\%)$
$4f_{7/2}^{-1}$						
1	0	0	2.66	11.3	2.78	7.4
2	0.92	0.93	4.58	8.4	4.70	6.0
6	0.95	0.94	12.79	1.6	12.85	1.2
3	1.50	1.52	6.44	8.0	6.68	4.5
4	1.91	1.91	8.79	2.4	8.87	1.4
5	1.95	1.96	10.99	0.1	10.99	0.1
$4f_{5/2}^{-1}$						
1	10.94/0	11.83/0	2.44	18.7	2.70	10.0
5	11.39/0.45	12.24/0.40	10.79	1.9	10.84	1.4
3	12.22/1.29	13.08/1.25	6.87	1.9	6.94	0.9
2	12.31/1.37	13.18/1.35	4.57	8.5	4.91	1.8
4	12.56/1.62	13.42/1.58	9.00	0.0	9.00	0.0
0	25.23/14.29	26.13/14.30	0.68	32.3	0.69	31.0

Table 4.1: Relative binding energies and relative intensities for the main peaks of the $4f$ XPS of U^{5+} using NESC/RASSI/AMFI compared to the full 4 component DCI results of Bagus et al. [16]. The orbitals of the final state were kept identical to the initial state. For the $4f_{5/2}$ peaks, also the energy relative to the first $4f_{5/2}$ peak is given. The relative intensities are summed over all M_J states. The percentage of intensity lost to satellites is also given.

J	$E_{\text{rel}}/\Delta E_{\text{rel}}(\text{eV})$	$E_{\text{rel}}^{4\text{C}}/\Delta E_{\text{rel}}^{4\text{C}}(\text{eV})$	I_{rel}	lost $I(\%)$	$I_{\text{rel}}^{4\text{C}}$	lost $I(\%)$
$4f_{7/2}^{-1}$						
1	0	0	2.50	16.7	2.67	11.1
2	1.10	1.08	4.30	14.0	4.58	8.3
6	1.15	1.11	12.00	7.69	12.80	1.5
3	1.78	1.75	6.07	13.3	6.44	8.0
4	2.25	2.22	8.25	8.3	8.79	2.3
5	2.29	2.26	10.30	6.4	10.99	0.1
$4f_{5/2}^{-1}$						
1	11.06/0	11.63/0	2.32	22.7	2.48	17.4
5	11.56/0.50	12.13/0.50	10.11	8.1	10.80	1.9
3	12.54/1.48	13.09/1.46	6.46	7.7	6.88	1.8
2	12.68/1.62	13.21/1.58	4.44	11.2	4.64	7.2
4	12.94/1.88	13.48/1.85	8.43	6.3	8.99	0.0
0	28.74/17.68	28.38/16.75	0.59	41.0	0.66	34.2

Table 4.2: Relative binding energies and relative intensities for the main peaks of the $4f$ XPS of U^{5+} using NESC/RASSI/AMFI compared to the full 4 component DF-SCF results of Bagus et al. [17]. The difference with respect to the results in Table 4.1 is that the orbitals of the final state were allowed to relax in the presence of the frozen core hole.

which the ionization takes place, were allowed to relax (Table 4.2). This allows us to estimate the effects due to orbital relaxation in the final state. We also include the results of the full four-component (4C) DCI and DF-SCF methods by Bagus and Ilton [17] for comparison.

The intensity of a level is summed over all M_J states. Therefore the maximum intensity of a given level is equal to its multiplicity ($2J + 1$). The intensity lost to satellites due to configuration mixing and orbital relaxation is given in the tables.

Both types of calculations show two dominant structures coming from the ionization from either the $4f_{7/2}$ (0 – 3 eV) or the $4f_{5/2}$ orbital (10 – 29 eV). There is excellent agreement in relative energies between the NESC/RASSI/AMFI results and the 4C results within the $4f_{7/2}^{-1}$ and $4f_{5/2}^{-1}$ structures, but the splitting between the two structures is 5 – 8% lower in our results: 0.9 eV without orbital relaxation and 0.5 eV with orbital relaxation. The relative intensities of the shown multiplets is lower in our results compared to the 4C results, which suggests more intensity “stealing” in our calculations.

Orbital relaxation has an effect on both the relative binding energies as well as the relative intensities. The splitting within both the $4f_{5/2}$ and the $4f_{7/2}$ structures increases. This is caused by the reduced shielding of the nuclear charge in the final state, which makes the 5f orbitals more compact, the 4f-5f Coulomb interactions larger, leading to larger splittings. There is also an overall decrease in intensity of the peaks, since orbital relaxation allows intensity “stealing” by satellites.

The differences in both the binding energies and intensities between our results and the 4C results can be attributed to two effects. The first is that the Gaunt interaction is included in an approximate way through the AMFI spin-orbit interaction. In a separate 4C calculation, we found that the inclusion of the Gaunt term in the 4C calculations reduces the splitting between the $4f_{7/2}^{-1}$ and $4f_{5/2}^{-1}$ structures by ≈ 0.4 eV.

The second is the fact that the spatial dependence of the $f_{5/2}$ and $f_{7/2}$ orbitals is the same in NESC/RASSI/AMFI. In the 4C calculations these orbitals are optimized with the spin-orbit interaction included in the Hamiltonian, therefore the spatial dependence is different. In our results, the 4f orbitals have approximately the spatial dependence of the average of the $4f_{5/2}$ and $4f_{7/2}$ orbitals. These orbitals are more similar to the $4f_{7/2}$ orbitals, because they contribute more to the average. This means that the effect of orbital relaxation is greater for the $4f_{5/2}$ orbitals, which results in a larger SO splitting. The difference in intensities can be explained by the similar spatial dependence of the 5f orbitals, which makes

the mixing of the $5f_{5/2}^1$ and $5f_{7/2}^1$ configurations more efficient in our calculations. Therefore more intensity is lost to satellites of $5f_{7/2}$ character, compared to the full 4C calculations.

4.3 Conclusions

The developed approach, as outlined in the previous chapters of this thesis, was benchmarked in the calculation of the 4f XPS spectra of U^{5+} cation for which the results of full four-component relativistic calculations are available [16, 17]. The multiplet splittings and the relative intensities of the 4f XPS spectra of U^{5+} calculated using the NESC/RASSI/AMFI approach are in a generally excellent agreement with the results of four-component calculations. A slight underestimation (*ca.* 10 %) of the magnitude of the splitting between the $4f_{5/2}$ and $4f_{7/2}$ states can be partly attributed to the inclusion of the Gaunt term in the AMFI method. The rest is attributed to the fact that the orbital optimization is being done in the presence of the spin-free Hamiltonian, which is an approximation. It may be surprising that the core spin-orbit splitting is actually so well reproduced in the RASSI/AMFI approach, which was designed to treat the SO splittings in the valence shells of compounds of heavy elements [56]. However the 4f shell is not a very deep core shell, and the approximations used in AMFI are still applicable to this sub-valence shell.

The relative intensities are well reproduced compared to the 4C computations, but our intensities are generally slightly lower. More intensity was lost due to the more effective mixing in of $5f_{7/2}^1$ configurations into the final states.

Chapter 5

Theoretical description of $L_{2,3}$ X-ray absorption in small titanium clusters

The experimental X-ray absorption spectra at the $L_{2,3}$ edge of size-selected Ti clusters have been investigated by Lau et al. [60]. The spectrum of bulk Ti shows two broad lines, which are attributed to excitations from the $2p_{3/2}$ and the $2p_{1/2}$ shells, (the L_3 and L_2 edge, respectively). Spectra of small clusters, consisting of three Ti atoms or more, show the same characteristics. The spectra of the single atom and dimer show however a much richer structure, and the assignment of peaks is not straightforward.

We have calculated the $2p$ XAS of the Ti_2^+ and Ti^+ ions. For comparison, we have also calculated the spectrum of a neutral Ti atom, which is very similar to the spectrum of the monomer cation, and compared it to the experimental spectrum of Ref. [100].

5.1 Computational details

The calculations of the XAS spectra were performed in the NESC / RASSI / AMFI framework, with a relativistic Atomic Natural Orbital (ANO) basis set. For the atomic calculations, a basis set of valence double zeta quality was chosen (ANO-RCC-VDZ).

The ground state of the Ti^+ ion was described by a CASSCF calculation, in which the three active electrons were distributed over the $3d$ and $4s$ orbitals, with their spins coupled to a total $S = 3/2$. The excited states were calculated using RASSCF, where the active space consisted of the $2p$ orbitals in the RAS3 space and the $4s$ and $3d$ orbitals in the RAS2 space. A total of 9 active electrons were included and at most 5 "excitations" from the RAS2 to the RAS3 space were allowed. For various spin symmetries ($S=1/2, 3/2$ or $5/2$), a state average calculation was

performed over all 630, 360 or 45 states, respectively. The various RASCF states were subsequently mixed under the influence of the spin-orbit (SO) operator in the RAS State Interaction method, resulting in the spin-orbit states along with the transition intensities from the initial states. It was necessary to include all three $2p$ orbitals in the active space, in order to reproduce the SO splitting between the $2p_{1/2}$ and $2p_{3/2}$ orbitals.

For the ground state of the neutral Ti atom we chose to keep the $4s$ orbital inactive. The two remaining active valence electrons were distributed over the $3d$ orbitals, coupled to a total spin $S = 1$. The excited states were calculated using RASSCF, where the active space consisted of the $2p$ orbitals in the RAS3 space and the $3d$ orbitals in the RAS2 space. Three separate state average calculations of different spin multiplicities were performed, in which 120 ($S=0$), 150 ($S=1$) and 30 ($S=2$) states were included. Again, the spin-orbit states and transition intensities were obtained from the subsequent RASSI calculation.

For the calculations on the Ti_2^+ dimer we chose the valence triple zeta quality basis set ANO-RCC-VTZ. In order to find the ground state of the dimer, calculations on the potential energy surfaces of various low-lying states have been performed using the CASSCF method, in which the seven valence electrons were distributed over bonding and anti-bonding combinations of the $3d$, $4s$ and $4p$ orbitals (18 orbitals total, i.e. (7,18)CASSCF). No relativistic effects were included and the orbitals were optimized for each state separately. Since the results of the CASSCF calculations were not conclusive about the identification of the ground state, also CASPT2 calculations on selected states were performed. The previous CASSCF wave functions were used as a basis in these CASPT2 calculations. We have included as a perturbation not only configurations involving excitations from the valence shell to the previously unoccupied orbitals, but also those involving excitations from the $3s$ and $3p$ orbitals.

To make the calculations of the XAS of the dimer feasible, the number of configurations had to be drastically reduced. In the initial state, we chose to include only the main configuration of the ground state ${}^6\Sigma_g (\sigma_g(3d)^1 \pi_u(3d)^2 \delta_g(3d)^2 \sigma_g(4s)^2)$. Keeping the $\sigma_g(4s)$ orbital inactive, this is denoted as (5,5)CASSCF. For the final states, the $2p$ orbitals of atom A were included in the RAS1 space, occupied with at least 5 electrons, while the RAS2 space remained the same as in the initial state, i.e. (11,8)RASSCF. Spin-orbit states and transition intensities were again obtained from the subsequent RASSI calculation.

5.2 Atomic titanium

The valence configuration of the ground state of the neutral Ti atom is correctly deduced from Madelung's $n+l$ rule [101] as $4s^23d^2$, which gives rise to a 3F ground state. This rule is only applicable to neutral atoms [102], and in fact the ground state of the atomic cation Ti^+ has a double open shell $4s^13d^2$ valence configuration, giving rise to a 4F ground state. The $2p$ XAS spectra of the neutral atom [100] and the cation [60] are very similar, with some minor differences in the structure of the peaks. This suggests that the different $4s$ occupations have little effect on the $2p$ XAS.

In our CASSCF calculation of the Ti^+ ion, we distribute 3 electrons, coupled to a total $S = 3/2$, in all possible ways over the $4s$ and $3d$ orbitals. This includes the $4s^03d^3$ configurations, but their contributions to the ground state were negligible. For the final states, a maximum of 5 electrons were distributed over the $2p$ orbitals as well as 4 electrons over the $4s$ and $3d$ orbitals. The possible configurations are $2p^54s^03d^4$, $2p^54s^13d^3$ and $2p^54s^23d^2$, as well as several configurations with fewer electrons in the $2p$ shell. The configurations with 0-4 electrons in the $2p$ shell contribute negligibly to the states of interest, but cannot be excluded due to the way the RASSCF wave function is defined. As a first approximation the absorption is a one-electron process, which would mean that, due to the Laporte selection rules [103], only the transitions to $2p^54s^13d^3$ and $2p^54s^23d^2$ will have any appreciable intensity. However, for these highly excited states there may be a large amount of configuration mixing, which makes it important to include all these configurations in the wave function expansion.

The calculation of the neutral Ti atom is computationally less demanding, since we can keep the $4s$ orbital inactive (i.e. doubly occupied in all configurations). The configuration is thus $3d^2$ for the initial state and $2p^53d^3$ for the final states.

In the spectra, it is hard to assess whether peaks originate from excitations from the $2p_{1/2}$ or the $2p_{3/2}$ orbital. The reason is twofold: first of all, the spin-orbit coupled wave function is defined in terms of spin-free many-electron wave functions and therefore the spin-orbit coupled orbitals are not defined in the calculation. Secondly, the spin-orbit splitting of the $2p$ orbitals is of similar size as the valence splitting in the $3d$ shell. The spin-orbit splitting is however very sensitive to changes in the speed of light c , contrary to the valence splitting. For reasons of analysis, a series of calculations was performed with decreasing values of c , to amplify relativistic effects like the spin-orbit coupling resulting in pulling apart

contributions from the different j -levels of the $2p$ orbitals.

5.3 Ti_2^+ molecule

The electronic structure of the ground state of transition metal dimers in general can only be described by methods with a high level treatment of electron correlation. A reason is that the bond is dominated by the $4s$ - $4s$ interaction, which leads to a bonding σ_g and an anti-bonding σ_u molecular orbital. The $3d$ orbitals can also form bonding and anti-bonding combinations ($\sigma_g, \pi_u, \delta_g$ and $\sigma_u, \pi_g, \delta_u$, respectively), but the interaction is much weaker than between the $4s$ orbitals. Consequently, there are numerous states with different $3d$ occupations which are very close in energy and it may be difficult to assess which of the states is actually the ground state. Configurations with different $3d$ occupations may also mix, which makes a multi-configurational approach a necessity.

When we consider the interaction of two Ti atoms in their ground state ($^3F, 3d^2 4s^2$), they will form a weakly bound system. There is however a low-lying 5F state ($3d^3 4s^1$) at 0.81 eV above the ground state [104], to which one or both atoms may be excited. The interaction of 3F - 5F and/or 5F - 5F atomic states may contribute to the bonding, leading to a more strongly bound system.

It has been shown by Bauschlicher et al. [105] that, in the Multi-Reference CI framework, the ground state of neutral Ti_2 is $^3\Delta_g$, with a bond length of 1.95 Å. This state arises mainly from the 5F - 5F interaction of the Ti atoms and it has a leading valence configuration $\sigma_g(3d)^1 \pi_u(3d)^4 \delta_g(3d)^1 \sigma_g(4s)^2$. From the Aufbau principle, it would be expected that the electronic configuration of the +1 charged species is similar to that of the neutral Ti_2 , with one electron removed from either the $\sigma_g(3d)$ or $\delta_g(3d)$ orbital. This would lead to a $^2\Delta_g$ or $^2\Sigma_g$ state, respectively. It has been suggested by Gutsev et al. that in the DFT framework [106] the ground state of Ti_2^+ is indeed a $^2\Delta_g$ state, with a bond length of 1.78 Å. In their work, it was however assumed that the spin multiplicity of the neutral molecule and the cation may only differ by 1 (the ± 1 rule). This means that no major redistribution of valence electrons over different $3d$ orbitals was possible, which is a serious approximation for a system with such a dense $3d$ manifold.

In our CASSCF calculation for Ti_2^+ , the valence $4s$ and $3d$ orbitals were included in the active space as well as the $4p$ orbitals, giving a total of 18 active orbitals. The resulting CASSCF potential energy surfaces of the lowest states of different (spin)

symmetry are shown in Fig. 5.1. The ground state according to these results is the ${}^6\Delta_g$ state, with a bond length of 3.4 Å. This state has a $\sigma_g(4s)^2\sigma_u(4s)^1$ occupation, with the remaining 4 electrons occupying various almost degenerate combinations of the 3d orbitals. The long bond length is due to the occupation of the anti-bonding $\sigma_u(4s)$ orbital. There are however various low-lying excited states within 0.2 eV above the ground state. Since the effects of dynamical correlation are underestimated in this CASSCF calculation, we need to go to a higher level of theory to be able to find the true ground state of the system.

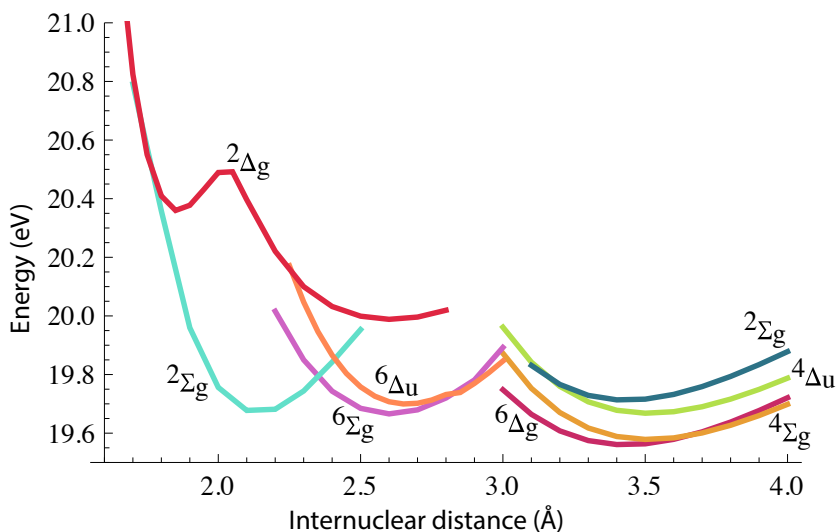


Figure 5.1: The potential energy surface of the various low-lying states of the Ti_2^+ dimer, calculated using 7-in-18 CASSCF.

We include a large part of the dynamical correlation by the CASPT2 method. It has been shown that the inclusion of the sub-valence 3s and 3p orbitals in the correlation treatment is important for the Ti dimer [107]. Starting from the CAS-SCF wave function (7 electrons in the valence 4s / 3d / 4p space), excitations from the valence space to the virtual space (5s and higher lying orbitals) and from the sub-valence (3s / 3p) to the valence and virtual space are included in the CASPT2 calculation.

From the CASPT2 results in Fig. 5.2, it can be seen that the inclusion of dynamic correlation has a different effect on the various states in the calculations.

The energetic effect is larger for the states with short bond lengths ($< 3.0 \text{ \AA}$), compared to the states with longer bond lengths ($> 3.0 \text{ \AA}$). The reason is that states with a long bond length have a singly occupied anti-bonding $4s$ orbital, at the cost of one less electron in the $3d$ manifold. Excitations from and to this more diffuse $4s$ orbital contribute less to the correlation energy than a similar $3d$ orbital. Also due to the extended bond length, the electrons are on average further apart, which reduces the amount of dynamical correlation. This is reflected in the higher weight of the CASSCF reference in the perturbed wave function (≈ 0.89 , versus $0.85 - 0.88$ for the states with lower bond length).

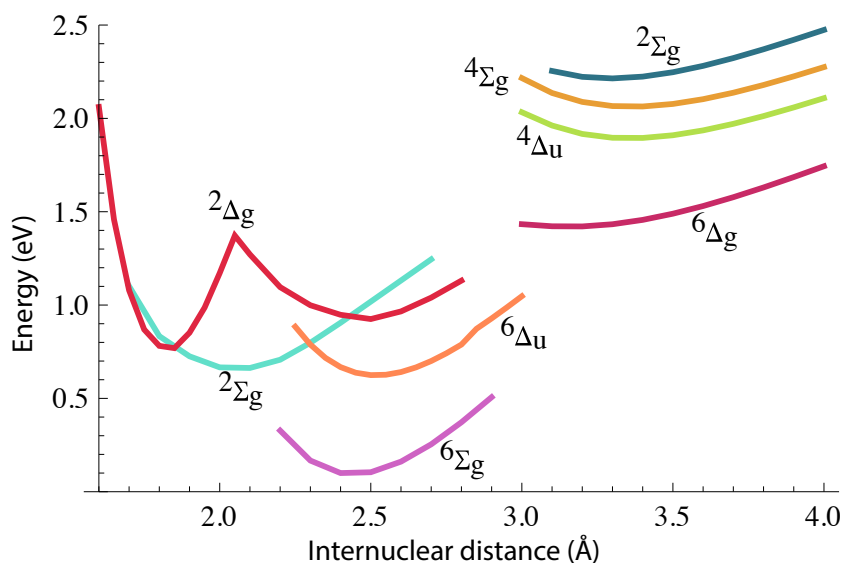


Figure 5.2: The potential energy surface of the various low-lying states of the Ti_2^+ dimer, calculated using the CASPT2 correction to the results of Fig. 5.1.

Among the states with lower bond lengths, the $6\Sigma_g$ and the first $2\Delta_g$ are stabilized more than the $2\Sigma_g$, $4\Sigma_g$ and second $2\Delta_g$ states. The reason for this is difficult to assess. It should be noted that the differences between states, on the order of 0.5 eV , is very small compared to the total dynamical correlation energies, which is about $18\text{--}20 \text{ eV}$. Nevertheless, experience has shown that energy differences of the order 0.5 eV are significant.

In both calculations, there is an interesting double well structure in the $2\Delta_g$

state. This is actually a combination of two states with a different electronic configuration, but the same spatial and spin symmetry, each with their own local minimum. These states cross at around 2.0 Å.

The ground state of the system was identified as the ${}^6\Sigma_g$ state with a bond length of 2.44 Å. The first excited state ${}^6\Delta_u$ lies 0.52 eV higher in energy and is almost degenerate with the ${}^2\Sigma_g$ state at 0.56 eV. The supposed ground state, ${}^2\Delta_g$, from previous DFT results [106] is actually the third excited state in our CASPT2 calculations. In the DFT study, the sextet states were left uninvestigated. The reason is that these results were based on the assumption that the ionization of the dimer is a one-electron process and that the spin multiplicity of the neutral and charged species may only differ by ± 1 . This assumption is false, since the ionization process does not generally result in the *ground state* of the ionized system. Our results show that the ground state of the cation is indeed reached by a redistribution of the valence electrons after ionization. The main configuration in the neutral species is $\sigma_g(3d)^1 \pi_u(3d)^4 \delta_g(3d)^1 \sigma_g(4s)^2$, which changes to $\sigma_g(3d)^1 \pi_u(3d)^2 \delta_g(3d)^2 \sigma_g(4s)^2$ (all bonding 3d orbitals singly occupied) for the charged species.

5.3.1 Symmetry breaking and localization

Some remarks about the treatment of symmetry in our calculations are in place. The wave functions transform according to the irreducible representations of the point group symmetry of the dimer, i.e. $D_{\infty h}$. However, especially in the description of core-hole states, a description in terms of symmetry-adapted molecular orbitals leads to the correct results only if a large number of configurations is included in the CI expansion [108]. A description in terms of localized, symmetry broken, orbitals leads to a better result (i.e. to lower energy), while using fewer configurations. In the case of the titanium dimer, the core-hole orbital may then localize on the first atom (A), which gives rise to relaxation of the electron cloud towards the increased effective charge which has been introduced on that atom. The symmetry-broken wave functions can be denoted as Ψ^A for the core-hole localized on atom A and, similarly, Ψ^B for atom B. Symmetry-adapted wave functions can then be expressed as

$$\Psi = \frac{1}{\sqrt{2 \pm 2S}} (\Psi^A \pm \Psi^B), \quad (5.1)$$

with S the overlap between the two wave functions $\langle \Psi^A | \Psi^B \rangle$. The interaction matrix element, as well as the overlap, between the symmetry-broken solutions involving deep core excitations localized on different atoms is very small. Consequently the plus/minus combinations of Eq. (5.1) are almost degenerate in our system and a sufficiently accurate description of the core-excited states can be obtained by the localized wave function.

A consequence is that we need to perform all calculations of the dimer in reduced symmetry, i.e. C_{2v} , including the initial state. The search for the ground state has been performed in the D_{2h} subgroup of $D_{\infty h}$. The ${}^6\Sigma_g$ ground state has also been calculated in the C_{2v} subgroup, which lacks the mirror plane connecting both atoms. In this calculation the titanium atoms are thus not related by symmetry and consequently the orbitals are not restricted to form strictly bonding and anti-bonding combinations. It was found that the CASSCF energy was lowered by 0.41 eV compared to the D_{2h} calculation. This stabilization was accompanied by a localization of the two singly occupied orthogonal $\delta_g(3d)$ orbitals, each onto one of the atoms. This left-right correlation has been taken into account in the D_{2h} calculation by inclusion of the anti-bonding $\delta_u(3d)$ into the active space. However, in the C_{2v} calculation an extra orbital shows up in the active space, since the left-right correlation has already been taken into account at the orbital level. The extra localized $4d$ orbitals act as correlating orbitals for the $3d$ orbitals and it is this effect that lowers the energy. Moreover, in the active space the anti-bonding $4p$ orbitals turned out to be replaced by bonding $\sigma_g(4d)$ and $\pi_u(4d)$ orbitals, which act as correlating orbitals for the $\sigma_g(3d)$ and $\pi_u(3d)$ orbitals. The CASPT2 energy obtained in C_{2v} symmetry was however increased by 0.63 eV compared to the D_{2h} calculation. It is clear that the stabilizing effect of the lower symmetry is an artifact caused by the increased freedom in choice of orbitals, especially the correlating orbitals. Therefore, we can safely assume that the ${}^6\Sigma_g$ state is indeed the true ground state of the system.

In the XAS calculation, the active space of the initial state has to be a subset (in our case, the valence orbitals) of the active space of the excited states in order to make it possible for the transition intensities to be calculated. The number of configurations of the excited states quickly grows out of hand when we increase the number of valence orbitals. The preferred active space of all $3d$ orbitals in RAS2 and the $2p$ orbitals of one of the atoms in RAS3 is too large to be computed. Therefore we need to choose a subset of the valence orbitals to be kept in the active space, while we keep the remainder of the valence space unoccupied. Since

the main configuration of the ${}^6\Sigma_g$ ground state is $\sigma_g(3d)^1\pi_u(3d)^2\delta_g(3d)^2\sigma_g(4s)^2$, i.e. all bonding $3d$ orbitals singly occupied, we choose to keep only the bonding combinations of the $3d$ orbitals in RAS2. Also, we put the $2p$ orbitals of one of the Ti atoms in the RAS1 space and allow at most single excitations from the RAS1 to the RAS2 space.

In C_{2v} symmetry, localization of the two $\delta_g(3d)$ orbitals in the initial state occurs also in this reduced active space. The original delocalized state may be constructed as a linear combination of the two localized states, similar to Eq. 5.1. The two localized states are related by symmetry in two ways: by the σ_h mirror plane as well as a rotation of 45 degrees around the interatomic axis. Since all $2p$ orbitals of one atom are active in our calculation, any rotation of the initial wave function around the interatomic axis does not influence the relative intensities of the final states. Therefore, we may assume that the impact of using the localized initial wave function, instead of the delocalized one, on the final spectrum will be negligible.

5.4 Results and discussion

In Figure 5.3 we show the calculated spectra of the neutral Ti atom for various values of the speed of light, c . At the true speed of light (≈ 137 a.u.), the peaks originating from excitations from the $2p_{1/2}$ (L_2 edge) or the $2p_{3/2}$ (L_3 edge) shells are not very well distinguishable. At lower c , the relativistic effects are amplified, which results in the L_2 edge to shift towards higher energies and become separated from the L_3 edge, which shifts only very slightly towards higher energies. It is now clear where the onset of the L_2 edge is located, as can be seen from the guide lines put on the first peak of significant intensity of the L_2 edge.

We have analyzed the character of the major contributions to the peaks in the spectra. The only possible final states for the neutral Ti atom are those corresponding to the $3d \leftarrow 2p$ excitation, i.e. those with a $2p^5 3d^3$ occupation. In terms of the mixed coupling scheme, the final states are constructed by coupling the possible Russell-Saunders terms of the $3d^3$ configuration, which are 4F , 4P , 2H , 2G , 2F , $2 \times {}^2D$ and 2P , to the core hole with $J = 1/2$ or $J = 3/2$. We have attempted the assignment for the $c = 100$ calculation in Fig. 5.3 only, since there the L_3 and L_2 structures are well separated. After careful examination of the distribution and multiplicities of the final states, we can assign the most intense peaks to

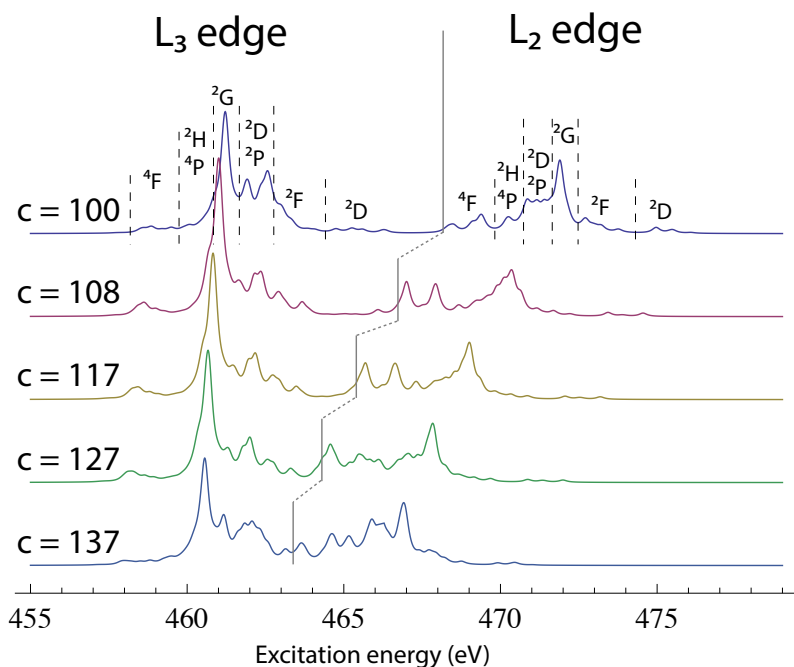


Figure 5.3: The dependence of the $2p$ XAS of the neutral Ti atom as a function of the speed of light c . Spectral lines have been broadened by a 0.3 eV FWHM Lorentzian to model the finite life-time of the excited states. At lower c , the distinction between the the L_3 and L_2 edges becomes clearer. The grey lines have been placed as a guide to the eye to show the onset of the L_2 edge.

the 2G term, coupled to the $2p_{1/2}$ or $2p_{3/2}$ core hole. Other major contributions are those originating from the coupling of the 2P and one of the 2D terms to the core hole. The other terms give rise to the satellite peaks and broad shoulders around the main peaks. Extrapolating these assignments to the $c = 137$ calculation is possible, but it should be noted that states of the same J -value may mix and the assignment of peaks is less straightforward than in the $c = 100$ calculation.

From these results, the apparent spin-orbit splitting of the $2p$ shell is 3.1 eV, which is about 0.5 eV smaller than the apparent spin-orbit splitting in the experimental spectrum (Fig. 5.4). The branching ratio has been calculated as the ratio of the sums of the calculated intensities of the L_3 and L_2 edges. The value of 1.09

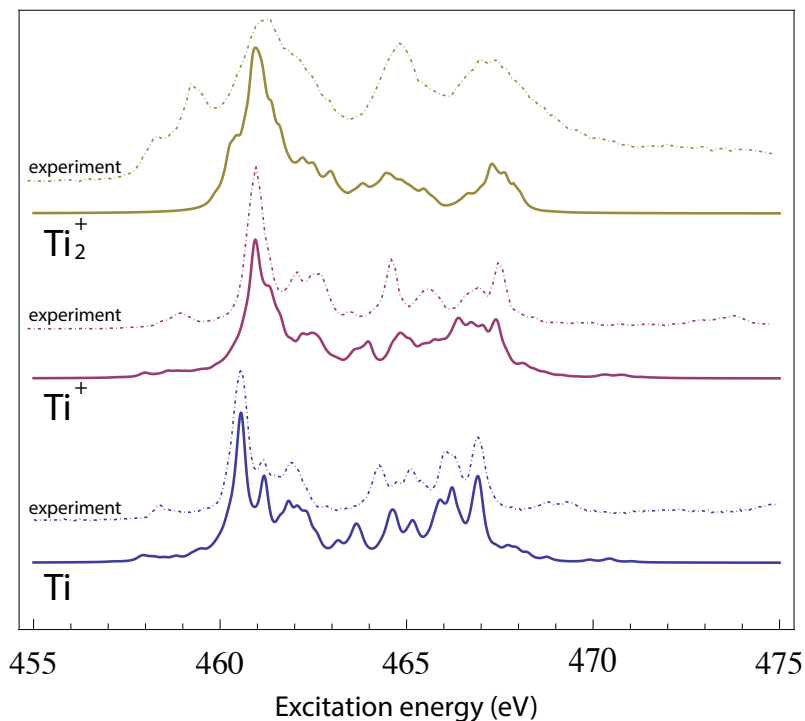


Figure 5.4: The calculated XAS spectra of the neutral atom (Ti), the mono-atomic cation (Ti^+) and the diatomic cation (Ti_2^+). The spectrum of Ti_2^+ has been shifted rigidly towards higher excitation energy by 3 eV to aid in the comparison. Spectral lines have been broadened by a 0.3 eV FWHM Lorentzian to model the finite life-time of the excited states. Included are the experimental spectra of Ti from Ref. [100] and of Ti^+ and Ti_2^+ from Ref. [60]. The experimental spectra have been shifted rigidly such that the most intense peaks are aligned with respect to the computed spectra.

deviates strongly from the statistical value of 2, which would be expected from the initial occupation numbers of the $2p$ orbitals ($n = 4$ and 2 for $j = 3/2$ and $1/2$, respectively). There are two reasons for this deviation. Firstly, the L_3 and L_2 structures are overlapping slightly, and some states belonging to the L_3 edge are wrongly attributed to the L_2 edge. The most important reason is however a many-electron effect. There is significant configuration mixing in the final states, such

that states cannot be described as pure $2p_{1/2}$ or $2p_{3/2}$ hole states. The branching ratio of the $c = 100$ calculation is 1.47, and the deviation from 2 results almost purely from this configuration mixing effect.

In Figure 5.4 we show the calculated $2p$ XAS spectra of the neutral Ti atom, Ti^+ ion and Ti_2^+ ion. The experimental spectra [60, 100] are included for comparison. The computed spectra of Ti^+ and neutral Ti look almost identical, other than some slight changes in intensities. The excitation energies of Ti^+ are however ≈ 0.4 eV higher than those of the neutral atom. There is very good agreement between the computed and experimental spectra of Ti and Ti^+ , except that the L_2 edge appears slightly broader in the computed spectra. Also, in the experimental spectrum of Ti^+ there is an intense peak at 460 eV (shifted to 464.5 eV in the figure), which is not well reproduced in the calculation. This peak actually consists of several peaks that are strongly overlapping in the experimental spectrum, while they are more separate in the computed spectrum.

The spectrum of the Ti_2^+ dimer has been shifted towards higher excitation energy by 3 eV to aid in the comparison to the Ti^+ spectrum. The peaks in the spectrum of Ti_2^+ appear broader compared to those of the Ti^+ spectrum. This is due to the larger number of valence shell states of similar energy. This broadening is underestimated when compared to the experimental spectrum, which is to be expected since we have only included a (small) subset of the valence space. For the same reason, some peaks at lower excitation energies do not appear in the calculated spectrum. The apparent spin-orbit splitting is about equal to the splitting in the Ti^+ spectrum, which is also the case in the experimental spectra.

5.5 Conclusions

We have shown the first results of ab-initio calculations of the X-ray absorption spectra of Ti clusters. The computed $2p$ XAS of the Ti atom is in very good agreement with the experimental spectra. In order to interpret the computational spectra, a computational experiment was performed by varying the speed of light. By lowering the speed of light in the calculation (Fig. 5.3), the relativistic effects, most prominently the spin-orbit splitting of the $2p$ shell, are amplified. The L_2 and L_3 structures are pulled apart to aid in the identification of the peaks in the spectrum. Even though this computational experiment is completely unphysical and cannot be performed in the real world, it is nevertheless very helpful in determining the

apparent spin-orbit coupling and $L_{2,3}$ branching ratio of the spectrum at the true speed of light.

The analysis revealed that the major peaks in the spectrum arise from the 2G state, coupled to the $2p_{1/2}$ and $2p_{3/2}$ core holes. Other large peaks arise from the 2P and one of the 2D states, coupled to the same core holes. The other states contribute to the spectrum as shoulders of the main peaks and as satellite peaks.

In the experimental 2p XAS of Ti^+ (Fig. 5.4), it seems that there are *three* major peaks, instead of the two which are expected from the SO splitting of the 2p core shell. Two of the major peaks are well reproduced in our calculations, but the intense peak at 460 eV in the experimental spectrum is not well reproduced. It seems that this peak is actually the result of coincidentally overlapping peaks of several transitions with comparable excitation energies. In the computed spectrum, these transitions are more apart in energy and hence appear more separate.

For the 2p XAS of the Ti_2^+ dimer, first a suitable initial (ground) state had to be found. At the CASSCF level, the potential energy curve computation (Fig. 5.1) showed that several states of comparable energy compete to be labelled as ground state. These states are very different in electronic structure and choosing the wrong initial state would result in a very different spectrum. By including more dynamical correlation effects with the CASPT2 computation (Fig. 5.2), the $^6\Sigma_g$ state was found to be the ground state. This is different than would be expected from the so-called ± 1 rule, as suggested for the multiplicities of ionized systems compared to their neutral counterparts [106]. The ± 1 rule fails to account for any redistribution of the electrons after the one-electron process of ionization. According to our calculations, the energy due to the redistribution of the valence electrons is so large in this system, that the energy ordering of the states in Ti_2^+ is very different from the ordering in the neutral dimer.

The calculated Ti_2^+ spectrum (Fig. 5.4) shows the same three main peaks as the experimental spectrum, although the intensities of the peaks at higher excitation energies are somewhat underestimated. This is to be expected from the fact that only a small part of the valence space is included in the calculation. That means that excitations to initially unoccupied orbitals with higher energy, which contribute to the high energy ends of the L_2 and L_3 structures, are missing from the computation. The high energy end of the L_3 edge overlaps with the L_2 edge, therefore the intensity is indeed missing in the expected part of the spectrum. The missing peaks below 460 eV can also be ascribed to excitations to unoccupied orbitals, presumably with a redistribution of the other valence electrons since the

excitation energy is so low.

In summary, this is the first demonstration that a computational XAS can be generated for a non-centrosymmetric system from first principles quantum chemical calculations. The computed spectrum for Ti_2^+ is sufficiently accurate to be able to interpret the experimental peaks.

Chapter 6

The 4p and 5p XPS of Ytterbium Phosphide¹

In the previous chapters, the developed method has only been applied to the calculation of single atoms, or diatomic molecules. In this chapter, we apply the method to the calculation of the 4p and 5p XPS of ytterbium in the crystalline solid ytterbium phosphide (YbP). The solid is modeled using the embedded cluster model, which means that only a small part of the solid (one atom or a small cluster) is described quantum-mechanically and the rest of the solid is represented by the electrostatic field it generates [109, 110]. This approach allows the ionization to take place locally on a single Yb^{3+} ion, while the oxidation states of all other Yb ions are left unchanged.

As a first approximation, we have computed the spectra of a single Yb^{3+} ion, embedded in the field of the surrounding lattice. This is essentially a single atom calculation in reduced symmetry, but it is nevertheless useful for the identification of the main peaks in the spectrum.

A more accurate calculation is performed by describing the system as an embedded YbP_6^{15-} cluster. Of particular interest is the role of charge-transfer (CT) from the six surrounding P^{3-} ions to the central Yb ion during the ionization. These CT states are expected to be stabilized due to the increased positive charge on the Yb ion after ionization and their contribution to the XPS is assessed.

6.1 Details of calculations

Ytterbium phosphide YbP has the rock salt crystal structure with the space group $\text{Fm}\bar{3}\text{m}$ and a lattice constant of $5.5461 \pm 0.0005 \text{ \AA}$ at 295 K [111]. The calculations

¹Parts of this chapter have been published in R. Klooster, R. Broer and M. Filatov *Chem. Phys.* **2012**, 395 [98]

were carried out in the embedded cluster approximation where a YbP_6^{15-} cluster (Y–B bond length 2.773 Å) was embedded in the field of an array of point charges. For comparison, the embedded cluster calculations were also carried out for a single Yb^{3+} cation embedded in the Madelung field of the lattice. The formal valences of the atoms in YbP (i.e. ± 3) were taken as the magnitudes of the point charges modeling the crystal lattice. The array of point charges of the length of five lattice constants in each crystallographic direction was constructed whereby the surface point charges were renormalized using Evjen's scheme [80].

To make the description of the immediate coordination sphere of the cluster (or Yb cation) more realistic, all the point charges within a radius of 7.5 Å from the central atom were replaced with the respective model potentials, generated according to the *ab initio* embedding model potential (AIEMP) scheme developed by Seijo and Barandiarán [110]. The potentials were obtained from fitting the potential of a single atomic ion, Yb or P, embedded in the array of atomic ions described by the same model potential. When modeling the charge distribution of the atomic ions, 15 spherical symmetric Gaussian-type functions were used on ytterbium and 11 functions on phosphorous.

The calculations employ the ANO-RCC-VDZP double-zeta polarized basis set for ytterbium [112] and phosphorous [113]. The initial state of the Yb^{3+} cation was calculated using the (13,7)CASSCF wave function whereby the 4f-orbitals of Yb occupied with 13 electrons are included into the active space. For the final states of the ionized Yb^{4+} , the (18,10)RASSCF calculations were carried out in which 13 electrons in 4f-orbitals are taken into the RAS2 and 5 electrons in 5p-orbitals are taken into the RAS3, for the case of the 5p-hole (5 electrons in 4p-orbitals, for the case of the 4p-hole). For the YbP_6^{15-} cluster, the RAS2 active space included 13 electrons in the 4f-orbitals of Yb and 24 electrons in the odd (*ungerade*) symmetry adapted linear combinations of the 3s and 3p-orbitals of P. For the ionized YbP_6^{14-} cluster, the so-obtained (37,19) active space in RAS2 was augmented by the (5,3) active space in RAS3. The latter was set up similarly to the Yb^{4+} cation. The RAS3 space was restricted to accommodate at least five electrons. In all final states, the core orbitals were kept frozen during the RASSCF calculations.

6.2 Results and discussion

The initial state valence configuration of Yb^{3+} is $4f^{13}$. This gives rise to a ${}^2F_{7/2}$ ground state and a ${}^2F_{5/2}$ excited state, split by 1.3 eV. This splitting is large enough to ensure that the system is completely in the ground state at room temperature. In the cluster the initial state splits further due to the octahedral environment by about 0.05 eV and the system can be described by a Boltzmann distribution over the lowest states.

Ionization takes place from the 4p or 5p shell with $j = 1/2$ or $3/2$, which couples to the initial $J = 7/2$ to yield XPS allowed states of $J = 3, 4$ and $J = 2, 3, 4, 5$, respectively. In the cluster, the increased charge on Yb after ionization stabilizes charge transfer (CT) configurations in which electrons of the surrounding P 3p orbitals are donated to the central Yb 4f orbital. These $\text{Yb}(4/5p^5 4f^{14})\underline{L}$ CT configurations can mix with the $\text{Yb}(4/5p^5 4f^{13})$ non-CT configurations and this may give rise to extra features in the spectrum. All orbitals, except the core orbital from which the ionization takes place, are optimized to minimize the average energy of all (non-CT and CT) states. The obtained peaks are broadened by a Gaussian and Lorentzian distribution to model the lifetime and Doppler broadenings. Moreover the spectrum is shifted rigidly so that the most intense peak aligns with the experimental peak.

The calculated 5p XPS is shown in Figure 6.1. Comparison with the experimental spectrum shows that the SO splitting between the $5p_{1/2}$ and $5p_{3/2}$ peaks is ~ 0.4 eV lower in the Yb^{3+} calculation and ~ 1.2 eV lower in the cluster. The SO splitting in the cluster is lower because the core-hole is slightly hybridized with the valence P orbitals. The computed relative intensities are very close to the 2:1 statistical weight ratio of $5p_{1/2}$ and $5p_{3/2}$. In the experimental spectrum the $5p_{1/2}$ peak is less intense than expected from the intensity of the $5p_{3/2}$ peak.

The difference in SO splitting in the 5p shell can be explained by the difference in radial dependence of the $5p_{1/2}$ and $5p_{3/2}$ orbitals, which is not taken into account in our method. See also the discussion of this effect in chapter 4. Indeed, when we calculate the energies of the 5p ionized states in the Yb^{3+} ion using a 4C scheme, the 5p SO splitting increases by 1–1.2 eV. In the atomic calculation, the error due to the incorrect radial behavior of the 5p orbitals is mostly compensated by the error due to the neglect of the direct crystal environment.

The difference in relative intensities between the two peaks can be attributed to the neglect of higher lying configurations. These can mix more with the $5p_{1/2}^{-1}$

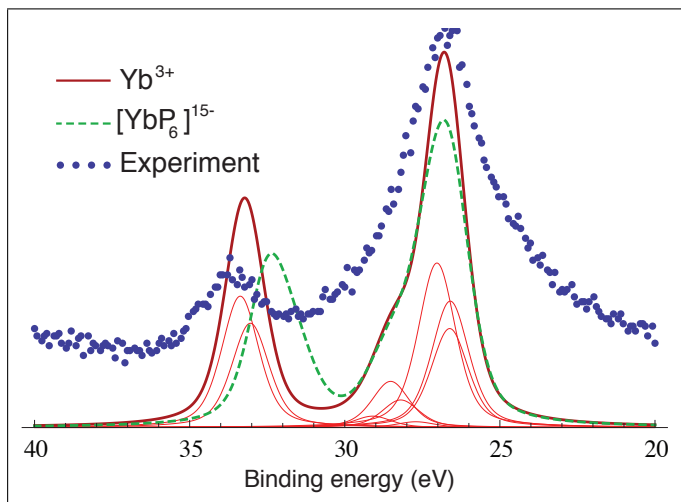


Figure 6.1: The calculated 5p XPS of Yb^{3+} and $[\text{YbP}_6]^{15-}$. The experimental spectrum has been taken from ref. [61].

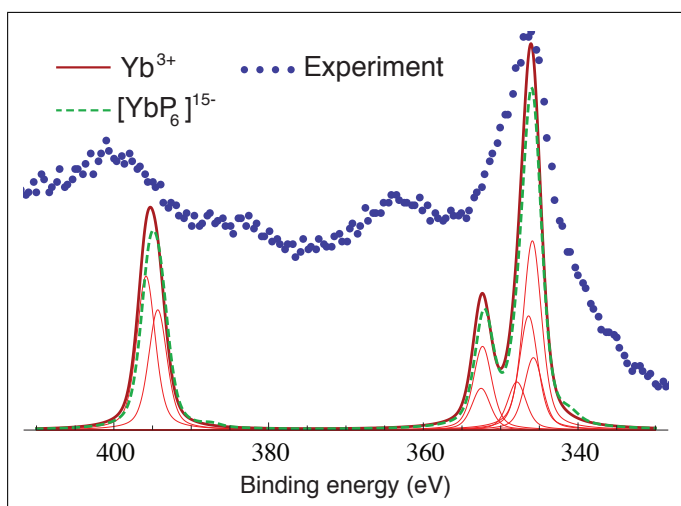


Figure 6.2: The calculated 4p XPS of Yb^{3+} and $[\text{YbP}_6]^{15-}$. The experimental spectrum has been taken from ref. [61].

states, and therefore “steal” more intensity from this peak.

The calculated 4p XPS is shown in Figure 6.2. The splitting between the $4p_{1/2}$

and the $4p_{3/2}$ structures is about 10 % (~ 6 eV) lower than the experimental splitting, while the splitting between the two peaks of the $4p_{3/2}$ structure is ~ 10 eV lower. In the cluster calculation the splittings are similar to the atomic calculation, but two extra peaks at 341 eV and 387 eV emerge which can be attributed to CT states. The binding energies of the CT states are thus lower than the non-CT states. The core ionization introduces extra positive charge on the Yb atom, which stabilizes those configurations in which an electron is transferred from a P 3p orbital to Yb 4f more than non-CT configurations. In the initial state, the CT states are only ~ 5 eV higher in energy than the ground state, so upon core ionization these drop below the non-CT states. The calculated intensity is very small, but it is expected that if the relaxation of a greater part of the crystal is taken into account, these contributions become more important.

The calculated binding energies of the Yb^{3+} ion have been compared to a full 4C calculation, which shows that the SO splitting of the core orbitals has been underestimated by about 4.5 eV in our NESC/RASSI/AMFI calculation, for the same reasons as in the 5p XPS. The splittings within the two structures, in particular within the $4p_{3/2}$ structure, were reproduced accurately, indicating that the treatment of relativistic effects is sufficiently accurate. The discrepancy between the experiment and our calculations may be explained by electron correlation effects, in particular the so-called frustrated Auger configurations which are missing in the present calculations. It has been shown [15, 18] that these configurations, in which there is a simultaneous excitation of a valence electron to a higher lying orbital and a de-excitation of an electron into the core-hole, may have a large effect on the relative binding energies.

In the experimental spectrum, the peak at 386 eV and the shoulder around 338 eV were attributed to surface Yb^{2+} contributions. From our calculations it can be seen that these may instead come from CT states.

6.3 Conclusions

In this chapter we have applied the developed method to the calculation of the 5p and 4p XPS of YbP, in the embedded cluster approximation. The results in this chapter show that the method for the calculation of XPS is indeed suitable for systems containing multiple atoms. This allows to go beyond the single atom description of the XPS process, and include multi-atom effects like ligand-to-

metal charge transfer.

The study of the 5p and 4p XPS of YbP has revealed that including a shell of ligand P atoms into the cluster has greater influence on the ionization of the sub-valence 5p shell, compared to the 4p shell. It was also found that ionization of the 4p shell is more sensitive to the effect of ligand-to-metal charge transfer, compared to the 5p shell. Charge transfer final states may be responsible for the occurrence of satellite peaks in the 4p XPS at 386 eV and at 338 eV which were previously attributed to the contribution of surface Yb^{2+} cations [61].

Bibliography

- [1] Siegbahn, K.; Nordling, C.; Fahlman, A.; Nordberg, R.; Hamrin, K.; Hedman, J.; Johansson, G.; Bergmark, T.; Karlsson, S.-E.; Lindgren, I.; Lindberg, B. *ESCA, Atomic, Molecular and Solid State Structure Studied by Means of Electron Spectroscopy*; Almqvist and Wiksell, Uppsala, 1967.
- [2] Siegbahn, K.; Nordling, C.; Johansson, G.; Hedman, J.; Hedén, P.; Hamrin, K.; Gelius, U.; Bergmark, T.; Werme, L.; Manne, R.; Baer, Y. *ESCA Applied to Free Molecules*; North-Holland Publishing Company, Amsterdam, 1969.
- [3] Ivashenko, O.; van Herpt, J.; Feringa, B.; Browne, W.; Rudolf, P. *Chemical Physics Letters* **2013**, *559*(0), 76 – 81.
- [4] Nordling, C.; Sokolowski, E.; Siegbahn, K. *Physical Review* **1957**, *105*, 1676–1677.
- [5] Whelan, C. M.; Cecchet, F.; Baxter, R.; Zerbetto, F.; Clarkson, G. J.; Leigh, D. A.; Rudolf, P. *The Journal of Physical Chemistry B* **2002**, *106*(34), 8739–8746.
- [6] Broer, R. In *Relativistic Methods for Chemists, Challenges and Advances in Computational Chemistry and Physics 10*; Barysz, M., Ishikawa, Y., Eds.; Springer, 2010; chapter 8.
- [7] Freeman, A. J.; Bagus, P. S.; Mallow, J. V. *International Journal of Magnetism* **1973**, *4*, 35–47.
- [8] Hozoi, L.; de Vries, A.; Broer, R.; de Graaf, C.; Bagus, P. *Chemical Physics* **2006**, *331*(1), 178 – 185.
- [9] Fujii, T.; de Groot, F. M. F.; Sawatzky, G. A.; Voogt, F. C.; Hibma, T.; Okada, K. *Physical Review B* **1999**, *59*, 3195–3202.
- [10] Stöhr, J. *NEXAFS Spectroscopy*, Springer Series in Surface Sciences; Springer, 1992.

- [11] Bressler, C.; Milne, C.; Pham, V.-T.; ElNahhas, A.; van der Veen, R. M.; Gawelda, W.; Johnson, S.; Beaud, P.; Grolimund, D.; Kaiser, M.; Borca, C. N.; Ingold, G.; Abela, R.; Chergui, M. *Science* **2009**, *323*(5913), 489–492.
- [12] Zhang, W.; Alonso-Mori, R.; Bergmann, U.; Bressler, C.; Chollet, M.; Galler, A.; Gawelda, W.; Hadt, R. G.; Hartsock, R. W.; Kroll, T.; Kjaer, K. S.; Kubicek, K.; Lemke, H. T.; Liang, H. W.; Meyer, D. A.; Nielsen, M. M.; Purser, C.; Robinson, J. S.; Solomon, E. I.; Sun, Z.; Sokaras, D.; van Driel, T. B.; Vanko, G.; Weng, T.-C.; Zhu, D.; Gaffney, K. J. *Nature* **2014**, *509*, 345–348.
- [13] Dirac, P. A. M. *Proceedings of the Royal Society of London A* **1928**, *117*, 610–624.
- [14] Bagus, P. S.; Broer, R.; de Jong, W. A.; Nieuwpoort, W. C.; Parmigiani, F.; Sangaletti, L. *Physical Review Letters* **2000**, *84*(10), 2259–2262.
- [15] Bagus, P. S.; Broer, R.; Ilton, E. S. *Chemical Physics Letters* **2004**, *394*, 150–154.
- [16] Ilton, E. S.; Bagus, P. S. *Physical Review B* **2005**, *71*, 195121.
- [17] Bagus, P. S.; Ilton, E. S. *Theoretical Chemistry Accounts* **2007**, *118*, 495–502.
- [18] Bagus, P. S.; Broer, R.; Ilton, E. S. *Journal of Electron Spectroscopy and Related Phenomena* **2008**, *165*, 46–49.
- [19] Bagus, P. S.; Freund, H.; Kuhlenbeck, H.; Ilton, E. S. *Chemical Physics Letters* **2008**, *455*(4–6), 331–334.
- [20] Swirles, B. *Proceedings of the Royal Society of London A* **1935**, *152*, 625–649.
- [21] Hafner, P. *Journal of Physics B: Atomic, Molecular and Optical Physics* **1980**, *13*, 3297–3309.
- [22] Adachi, H.; Ogasawara, K. In *DV-X α for Advanced NANO materials and other Interesting Topics in Materials Science*; Brandas, E. J., Adachi, H., Uda, M., Sekine, R., Eds., Vol. 42 of *Advances in Quantum Chemistry*; Academic Press, 2003; pages 1–22.
- [23] Ohno, M. *Journal of Electron Spectroscopy and Related Phenomena* **2003**, *131–132*(0), 3–28.
- [24] van der Laan, G.; Moore, K. T.; Tobin, J. G.; Chung, B. W.; Wall, M. A.; Schwartz, A. J. *Physical Review Letters* **2004**, *93*, 097401.
- [25] Moore, K.; van der Laan, G.; Tobin, J.; Chung, B.; Wall, M.; Schwartz, A. *Ultramicroscopy* **2006**, *106*(4–5), 261–268.
- [26] Moore, K. T.; van der Laan, G. *Reviews of Modern Physics* **2009**, *81*, 235–298.
- [27] Cowan, R. *The Theory of Atomic Structure and Spectra*, Los Alamos Series in Basic and Applied Sciences Series; University of California Press, 1981.

- [28] Thole, B. T.; van der Laan, G. *Physical Review A* **1988**, *38*, 1943–1947.
- [29] Thole, B. T.; van der Laan, G. *Physical Review B* **1988**, *38*, 3158–3171.
- [30] van der Laan, G.; Thole, B. T. *Physical Review Letters* **1988**, *60*, 1977–1980.
- [31] van der Laan, G.; Thole, B. *Journal of Electron Spectroscopy and Related Phenomena* **1997**, *86*(1–3), 57 – 63.
- [32] Bagus, P. S.; Ilton, E. S. *Physical Review B* **2006**, *73*, 155110.
- [33] Bagus, P. S.; Broer, R.; de Graaf, C.; Nieuwpoort, W. *Journal of Electron Spectroscopy and Related Phenomena* **1999**, *98*ñ99(0), 303 – 319.
- [34] Nelin, C. J.; Bagus, P. S.; Brown, M. A.; Sterrer, M.; Freund, H.-J. *Angewandte Chemie International Edition* **2011**, *50*(43), 10174–10177.
- [35] Ilton, E. S.; Bagus, P. S. *Surface Science* **2008**, *602*(5), 1114 – 1121.
- [36] Bagus, P. S.; Broer, R.; Parmigiani, F. *Chemical Physics Letters* **2006**, *421*(1ñ3), 148 – 151.
- [37] Ilton, E. S.; de Jong, W. A.; Bagus, P. S. *Physical Review B* **2003**, *68*, 125106.
- [38] Bagus, P. S.; Pacchioni, G.; Parmigiani, F. *Physical Review B* **1991**, *43*, 5172–5175.
- [39] Bagus, P. S.; Pacchioni, G. *Physical Review B* **1993**, *48*, 15274–15282.
- [40] Hermann, K.; Bagus, P. S.; Nelin, C. J. *Physical Review B* **1987**, *35*, 9467–9473.
- [41] Bagus, P. S.; Pacchioni, G.; Philpott, M. R. *The Journal of Chemical Physics* **1989**, *90*(8), 4287–4295.
- [42] Bagus, P. S.; Illas, F. *Chemical Physics Letters* **1994**, *224*(5–6), 576 – 580.
- [43] Bagus, P. S.; Ilton, E. S.; Nelin, C. J. *Surface Science Reports* **2013**, *68*(2), 273 – 304.
- [44] Josefsson, I.; Kunnus, K.; Schreck, S.; Föhlisch, A.; de Groot, F.; Wernet, P.; Odelius, M. *The Journal of Physical Chemistry Letters* **2012**, *3*(23), 3565–3570.
- [45] Kunnus, K.; Josefsson, I.; Schreck, S.; Quevedo, W.; Miedema, P. S.; Techert, S.; de Groot, F. M. F.; Odelius, M.; Wernet, P.; Föhlisch, A. *The Journal of Physical Chemistry B* **2013**, *117*(51), 16512–16521.
- [46] Okada, K.; Kotani, A.; Thole, B. *Journal of Electron Spectroscopy and Related Phenomena* **1992**, *58*(4), 325 – 343.
- [47] Okada, K.; Kotani, A. *Journal of the Physical Society of Japan* **1992**, *61*(12), 4619–4637.
- [48] Taguchi, M.; Uozumi, T.; Kotani, A. *Journal of the Physical Society of Japan* **1997**, *66*(1), 247–256.

- [49] Ikeno, H.; Tanaka, I.; Miyamae, T.; Mishima, T.; Adachi, H.; Ogasawara, K. *Materials Transactions* **2004**, *45*(5), 1414–1418.
- [50] Ikeno, H.; Tanaka, I.; Koyama, Y.; Mizoguchi, T.; Ogasawara, K. *Physical Review B* **2005**, *72*, 075123.
- [51] Ikeno, H.; Mizoguchi, T.; Tanaka, I. *Physical Review B* **2011**, *83*, 155107.
- [52] Barysz, M.; Syrocki, Ł. *Molecular Physics* **2014**, *112*, 583–591.
- [53] Barysz, M.; Mentel, Ł.; Leszczyński, J. *The Journal of Chemical Physics* **2009**, *130*(16), 164114.
- [54] Dyall, K. G. *The Journal of Chemical Physics* **1997**, *106*, 9618–9626.
- [55] Dyall, K. G. *Journal of Computational Chemistry* **2002**, *23*, 786–793.
- [56] Malmqvist, P. Å.; Roos, B. O.; Schimmelpfennig, B. *Chemical Physics Letters* **2002**, *357*, 230–240.
- [57] Schimmelpfennig, B.; Maron, L.; Wahlgren, U.; Teichteil, C.; Fagerli, H.; Gropen, O. *Chemical Physics Letters* **1998**, *286*, 267–271.
- [58] Åberg, T. *Physical Review* **1967**, *156*, 35–41.
- [59] Hermsmeier, B. D.; Fadley, C. S.; Sinkovic, B.; Krause, M. O.; Jimenez-Mier, J.; Gerard, P.; Carlson, T. A.; Manson, S. T.; Bhattacharya, S. K. *Physical Review B* **1993**, *48*, 12425–12437.
- [60] Lau, J. T.; Rittmann, J.; Zamudio-Bayer, V.; Vogel, M.; Hirsch, K.; Klar, P.; Lofink, F.; Möller, T. *Physical Review Letters* **2008**, *101*, 153401.
- [61] Saitoh, Y.; Suga, S.; Matsubara, H.; Tsukikawa, Y.; Mori, Y.; Oyamada, A.; Ochiai, A.; Suzuki, T.; Kasuya, T. *Journal of the Physical Society of Japan* **1991**, *60*, 4005–4008.
- [62] Roothaan, C. C. J. *Reviews of Modern Physics* **1951**, *23*, 69–89.
- [63] Hall, G. G. *Proceedings of the Royal Society of London A* **1951**, *205*(1083), 541–552.
- [64] Brillouin, L. *Les champs self-consistents de Hartree et de Fock*; Hermann, Paris, 1934.
- [65] Wolf, A.; Reiher, M.; Hess, B. A. *The Journal of Chemical Physics* **2002**, *117*(20), 9215–9226.
- [66] Wolf, A.; Reiher, M.; Hess, B. In *Relativistic Electronic Structure Theory. Part 1. Fundamentals*; Schwerdfeger, P., Ed.; Elsevier, Amsterdam, 2002; page 622.
- [67] Reiher, M.; Wolf, A. *The Journal of Chemical Physics* **2004**, *121*(5), 2037–2047.
- [68] Liu, W. *Molecular Physics* **2010**, *108*(13), 1679–1706.

- [69] Iliáš, M.; Saue, T. *The Journal of Chemical Physics* **2007**, *126*(6), 064102.
- [70] Iliáš, M.; Kellö, V.; Urban, M. *Acta Physica Slovaca* **2010**, *60*(3), 259–391.
- [71] Barysz, M. In *Relativistic Methods for Chemists, Challenges and Advances in Computational Chemistry and Physics 10*; Barysz, M., Ishikawa, Y., Eds.; Springer, 2010; pages 165–190.
- [72] Barysz, M.; Sadlej, A. J. *Journal of Molecular Structure: THEOCHEM* **2001**, *573*(1–3), 181 – 200.
- [73] Barysz, M.; Sadlej, A. J. *The Journal of Chemical Physics* **2002**, *116*(7), 2696–2704.
- [74] Reiher, M.; Wolf, A. *Relativistic Quantum Chemistry*; Wiley-VCH, 2009.
- [75] Filatov, M.; Dyllal, K. G. *Theoretical Chemistry Accounts* **2007**, *117*, 333–338.
- [76] Neese, F. *The Journal of Chemical Physics* **2005**, *122*(3), 034107.
- [77] Schimmelpfennig, B. private communication.
- [78] Fleig, T.; Olsen, J.; Visscher, L. *The Journal of Chemical Physics* **2003**, *119*(6), 2963–2971.
- [79] Kantorovich, L. N.; Tupitsyn, I. I. *Journal of Physics: Condensed Matter* **1999**, *11*, 6159.
- [80] Evjen, H. M. *Physical Review* **1932**, *39*, 675–687.
- [81] Huzinaga, S.; Cantu, A. A. *The Journal of Chemical Physics* **1971**, *55*, 5543.
- [82] Höjler, G.; Chung, J. *International Journal of Quantum Chemistry* **1978**, *14*, 623.
- [83] Pascual, J. L.; Barros, N.; Barandiarán, Z.; Seijo, L. *The Journal of Physical Chemistry A* **2009**, *113*, 12454.
- [84] Domingo, A.; Rodríguez-Forteza, A.; Swart, M.; de Graaf, C.; Broer, R. *Physical Review B* **2012**, *85*, 155143.
- [85] Briggs, D.; Seah, P. *Practical surface analysis: by auger and x-ray photo-electron spectroscopy*; Wiley, 1983.
- [86] Bayer, V.; Podloucky, R.; Franchini, C.; Allegretti, F.; Xu, B.; Parteder, G.; Ramsey, M. G.; Surnev, S.; Netzer, F. P. *Physical Review B* **2007**, *76*, 165428.
- [87] Fadley, C. S. *Surface and Interface Analysis* **2008**, *40*(13), 1579–1605.
- [88] Herzberg, G. *Molecular Spectra and Molecular Structure*; Van Nostrand, Princeton, 1950.
- [89] Domingo, A.; Rodríguez-Forteza, A.; Swart, M.; de Graaf, C.; Broer, R. *Physical Review B* **2012**, *85*, 155143.

- [90] Jolly, W. L. In *Electron Spectroscopy: Theory, Techniques and Applications I*; Brundle, C. R., Baker, A. D., Eds.; Academic, New York, 1977.
- [91] Saldin, D. K.; Ueda, Y. *Physical Review B* **1992**, *46*, 5100–5109.
- [92] Nuroh, K. *Physical Review B* **2008**, *78*, 245116.
- [93] De Francesco, R.; Stener, M.; Causa, M.; Toffoli, D.; Fronzoni, G. *Physical Chemistry Chemical Physics* **2006**, *8*, 4300–4310.
- [94] Šipr, O.; Šimůnek, A.; Bocharov, S.; Kirchner, T.; Dräger, G. *Physical Review B* **1999**, *60*, 14115–14127.
- [95] Poumellec, B.; Cortes, R.; Sanchez, C.; Berthon, J.; Fretigny, C. *Journal of Physics and Chemistry of Solids* **1993**, *54*(6), 751–763.
- [96] Uozumi, T.; Okada, K.; Kotani, A.; Durmeyer, O.; Kappler, J. P.; Beaurepaire, E.; Parlebas, J. C. *EPL (Europhysics Letters)* **1992**, *18*(1), 85.
- [97] Paunch, R. *Spin eigenfunctions*; Plenum Press, New York, 1979.
- [98] Klooster, R.; Broer, R.; Filatov, M. *Chemical Physics* **2012**, *395*, 122–127.
- [99] Roos, B. O.; Lindh, R.; Malmqvist, P.-Å.; Veryazov, V.; Widmark, P.-O. *Chemical Physics Letters* **2005**, *409*, 295–299.
- [100] Martins, M.; Godehusen, K.; Richter, T.; Wernet, P.; Zimmermann, P. *Journal of Physics B: Atomic, Molecular and Optical Physics* **2006**, *39*, R79.
- [101] Madelung, E. *Mathematische Hilfsmittel des Physikers*; Springer: Berlin, 3rd ed., 1936.
- [102] Goudsmit, S. A.; Richards, P. I. *Proceedings of the National Academy of Sciences* **1964**, *51*(4), 664.
- [103] Laporte, O.; Meggers, W. F. *Journal of the Optical Society of America* **1925**, *11*(5), 459.
- [104] Moore, C. E. *Atomic Energy Levels*, Vol. 1 and 2; Natl. Bur. Stand. (U.S.) Circ., 1949.
- [105] Bauschlicher, C. W.; Partridge, H.; Langhoff, S. R.; Rosi, M. *The Journal of Chemical Physics* **1991**, *95*(2), 1057.
- [106] Gutsev, G. L.; Bauschlicher, C. W. *The Journal of Physical Chemistry* **2003**, *107*, 4755.
- [107] Hübner, O.; Himmel, H.-J.; Manceron, L.; Klopfer, W. *The Journal of Chemical Physics* **2004**, *121*(15), 7195.
- [108] Ågren, H.; Bagus, P. S.; Roos, B. O. *Chemical Physics Letters* **1981**, *82*(3), 505.
- [109] Shukla, A.; Dolg, M.; Stoll, H.; Fulde, P. *Chemical Physics Letters* **1996**, *262*, 213–218.

- [110] Seijo, L.; Barandiarán, Z. In *Computational Chemistry: Reviews of Current Trends*; Leszczynski, J., Ed., Vol. 4; World Scientific, Singapore, 1999; pages 55–152.
- [111] Dönni, A.; Fischer, P.; Furrer, A.; Bonville, P.; Hulliger, F.; Ott, H. R. *Zeitschrift für Physik B Condensed Matter* **1990**, *81*, 83–88.
- [112] Roos, B. O.; Lindh, R.; Malmqvist, P.-V.; Veryazov, V.; Widmark, P.-O. *The Journal of Physical Chemistry A* **2008**, *112*, 11431–11435.
- [113] Roos, B. O.; Lindh, R.; Malmqvist, P.-V.; Veryazov, V.; Widmark, P.-O. *The Journal of Physical Chemistry A* **2005**, *108*, 2851–2858.

Samenvatting

Het ontwerpen van nieuwe (multi)functionele materialen is voor een groot deel gebaseerd op kennis van de microscopische eigenschappen van deze materialen, die op hun beurt voor een groot deel bepaald worden door de elektronische structuur. De elektronische structuur omvat de elektronische energieniveaus en bijbehorende elektronenverdelingen. Spectroscopie van binnenschilelektronen is een waardevolle techniek om de elektronische structuur van verschillende systemen, zoals atomen, moleculen en vaste stoffen, te achterhalen. De benodigde straling bevindt zich in het röntgengebied, vaak aangeduid als X-rays. De verschillende vormen van deze techniek kunnen worden ingedeeld in twee categorieën, namelijk X-ray foto-elektron spectroscopie (XPS) en X-ray absorptie spectroscopie (XAS).

Bij XPS wordt het systeem geïoniseerd met behulp van röntgenstraling met een vaste golflengte en de kinetische energie van de uitgestoten binnenschilelektronen gemeten. De bindingsenergie van die elektronen is het verschil van de energie van de straling en de kinetische energie. Bij XAS wordt gebruik gemaakt van röntgenstraling om een elektron van de binnenschil naar een valentieshil te exciteren. Door deze overgang wordt de röntgenstraling met een energie gelijk aan de excitatie-energie geabsorbeerd.

De bindingsenergie van een binnenschilelektron wordt in hoge mate bepaald door de kernlading van het atoom waarop het elektron zich bevindt. Daarom kan XPS gebruikt worden om de elementaire samenstelling van een systeem te bepalen. De bindingsenergieën worden daarnaast beïnvloed door oxidatietoestand en de chemische omgeving van het atoom. XAS wordt niet alleen beïnvloed door de binnenschil, maar ook door de valentieshil waar het elektron in terecht

komt. Doordat er veel meer overgangen mogelijk zijn, levert dit over het algemeen een rijker spectrum op dan bij XPS. Dus ondanks dat XPS en XAS overgangen van binnenschilelektronen omvat, bieden de resulterende spectra juist veel inzicht in de valentie-elektronische structuur van het systeem.

De interpretatie van de spectra kan, afhankelijk van het systeem en de binnenschil van interesse, erg ingewikkeld zijn. De simpelste modellen gaan uit van de verandering van de effectieve kernlading, doordat de afscherming door de elektronen verandert, om bijvoorbeeld verschillende oxidatietoestanden te beschrijven. Dit soort modellen negeert de expliciete interactie van het binnenschilelektron met de andere elektronen.

In dit proefschrift beschrijven we het XPS / XAS proces nauwkeuriger op basis van de eerste beginselen (*ab initio*) met kwantummechanica. In de kwantummechanica wordt de elektronische structuur van een systeem beschreven met een golffunctie Ψ , waaruit alle eigenschappen van dat systeem bepaald kan worden. Voor de beschrijving van een spectrum is het nodig de bindings- of excitatie-energieën en de overgangswaarschijnlijkheden te berekenen. Dit doen we door de golffunctie van het systeem voor en na de excitatie of ionisatie uit te rekenen met behulp van de tijdsonafhankelijke Schrödingervergelijking, $\hat{H}\Psi = E\Psi$. De Hamiltoniaan \hat{H} bevat alle fysische interacties in het systeem en door de vergelijking op te lossen wordt naast de golffunctie Ψ ook de energie E behorend bij deze golffunctie verkregen. De bindings- of excitatie-energie is het verschil van deze energie voor de begin- en eindtoestand.

De overgangswaarschijnlijkheid wordt voor XAS berekend met behulp van het overgangsdipoolmoment tussen de golffuncties van begin- en eindtoestand. Voor XPS is dit niet mogelijk, aangezien de golffuncties van begintoestand en geïoniseerde toestand een verschillend aantal elektronen bevatten. Daarom wordt er gebruikt gemaakt van de "Sudden Approximation" (Plotselinge Benadering), waarin aangenomen wordt dat de energie van de inkomende straling zo hoog is dat de overgang naar de geïoniseerde toestand instantaan verloopt. Er wordt een nieuwe "bevroren" golffunctie gedefinieerd, identiek aan de begintoestand maar met een elektron verwijderd uit een binnenschil. De overgangswaarschijnlijkheid wordt dan bepaald met behulp van de overlap van de bevroren golffunctie met de golffunctie van de eindtoestand.

Uit het voorgaande blijkt dat het essentieel is om de belangrijke fysische interacties in de Hamiltoniaan mee te nemen voor een goede beschrijving van een binnenschilelektronspectrum. Omdat de binnenschilelektronen met grote snel-

heid kunnen bewegen, zijn met name de effecten van relativiteit van belang. Voor de beschrijving van relativiteit in de kwantummechanica wordt doorgaans gebruik gemaakt van de Diracvergelijking. Hierbij bestaat de golf functie uit vier componenten: voor zowel het elektronische deel als het positronische deel van de golf functie een twee-componenten spinor die de spin van de elektronen beschrijft. Dit zorgt ervoor dat het formalisme rekenkundig dusdanig intensief wordt dat het alleen toegepast kan worden op kleine systemen. Daarom gebruiken we in dit proefschrift een getransformeerde vorm van de Diracvergelijking, met behulp van de genormaliseerde eliminatie van de kleine component (NESC), waarbij er maar één component overblijft. Hierdoor wordt het scalaire deel van de relativiteit op het een-elektronniveau toegevoegd, waar het de meeste invloed heeft, en kan de veel-elektrongolf functie berekend worden met "gewone" niet-relativistische methoden. Doordat de verschillende spin-componenten niet in de golf functie zitten, wordt de relativistische spin-baan koppeling nog niet meegenomen. Deze spin-baan koppeling, die belangrijk is voor valentieschillen van zware elementen en binnenschillen van vrijwel alle elementen, wordt aan het eind van de berekening toegevoegd aan de veel-elektrongolf functie.

Een ander belangrijke voorwaarde voor de nauwkeurige beschrijving van binenschilelektronspectra is het in rekening brengen van elektroncorrelatie. Dit is de specifieke interactie tussen de elektronen, naast de interactie van een elektron met het gemiddelde elektrostatische veld van de andere elektronen. Doordat we de golf functie terug hebben gebracht tot een één-component vorm, kunnen we gebruik maken van de uitgebreide gereedschapsset van de niet-relativistische kwantumchemie om elektroncorrelatie nauwkeurig te beschrijven.

Hoofdstuk 2 van dit proefschrift beschrijft de niet-relativistische en relativistische theorieën zoals deze gebruikt worden in de berekeningen. De toepassing van de theorie op het beschrijven van de XPS en XAS processen en de berekening en interpretatie van de spectra staat beschreven in hoofdstuk 3.

In hoofdstuk 4 passen we het formalisme toe op de berekening van de 4f XPS van het uranium(V) atoom. Aan dit systeem zijn vier-componenten berekeningen gedaan, waarmee onze resultaten worden vergeleken. De effecten van elektroncorrelatie en relaxatie van de elektronenbanen na ionisatie worden behandeld.

In hoofdstuk 5 berekenen we de 2p XAS van het titanium atoom, het Ti^+ ion en het Ti_2^+ molecuul. Experimentele spectra van deze systemen zijn gebruikt om de resultaten mee te vergelijken. Met name het Ti_2^+ systeem is interessant, omdat het de eerste keer is dat van een niet-centrosymmetrisch systeem het XAS berekend

wordt. De gevolgen voor de symmetrie in de eindtoestanden worden uitvoering beschreven.

In hoofdstuk 6 wordt het 4p en 5p XAS van ytterbium in YbP berekend. Hierbij maken we gebruik van het embedded-clustermodel, waarbij het materiaal beschreven wordt met een klein cluster omsloten door een elektrostatisch veld dat de rest van het kristal beschrijft. Het effect van de grootte van het cluster, met name het al dan niet meenemen van ligand–metaal ladingsoverdracht, wordt behandeld.

Acknowledgements

This project would not have been possible without the help and support of a lot of people.

First of all I would like to thank my promotor Ria Broer. Ria, ondanks je drukke agenda heb je altijd de tijd gevonden om te discussiëren over het project. Je hebt me gemotiveerd om dit proefschrift af te maken en daarvoor ben ik je dankbaar.

I thank Michael Filatov for raising my interest in relativistic quantum chemistry and supervision during the first years of my PhD project.

Thank you, Paul Bagus for interesting discussions during your frequent visits to our group in Groningen.

I would like to thank the reading committee, Luuk Visscher, Frank de Groot and Petra Rudolf, for taking the time to review my thesis and giving valuable feedback.

I have been around the Theoretical Chemistry group for over 10 years, starting with a Bachelor project supervised by Robert van Leeuwen. Bedankt Robert, dat je me hebt geïntroduceerd in het vakgebied en hebt geholpen met mijn eerste stappen in het programmeren in Fortran. Ik wil ook Paul de Boeij bedanken voor zijn uitstekende supervisie gedurende mijn Masterproject, wat mij heeft overtuigd om dit promotietraject te starten. Wim en Piet, jullie discussies en suggesties, met name tijdens de werkbesprekingen, waren erg waardevol. I would like to thank all other past and present group members for contributing to the nice atmosphere in the group: Remco, Johan, Gerrit-Jan, Andrii, Muizz, Hilde, Coen, Henriët, Dani, Daniel, Andranik, Reshmi, Adrian, Olena, Khompat, Rémi, Christian, Hossein, Alexandrina, Arjan, Pina, Meta, Nils, Maya, Javier and Tuomas.

Een speciaal woord van dank voor mijn huidige werkgever, HZPC. Hans en Robert, bedankt dat jullie me de mogelijkheid en tijd hebben gegeven om dit werk af te maken.

Muziek is altijd een belangrijk onderdeel van mijn leven geweest. Door de muziek heb ik een hoop mensen leren kennen tijdens mijn studie en promotie, die me eraan hielpen herinneren dat het leven niet alleen om werk draait. Alle mensen van Harmonie '67, Cover, Sun by Night / The Villains, Threshold Project en Sostenuto, bedankt!

Daarnaast wil ik al mijn vrienden en (schoon)familie bedanken voor hun steun tijdens dit project, ondanks dat ik niet altijd kon uitleggen waar het over ging. Egon, Maarten, Mark en Thom, zonder jullie had mijn studietijd er heel wat saaier uitgezien en ik ben blij dat we elkaar na de studie nog steeds regelmatig zien. Tijn, bedankt dat je er altijd voor me was in de afgelopen (ruim) 20 jaar. Mam, Nienke en Els, jullie hebben me altijd gesteund en aangemoedigd om dit boekje af te maken en ik hoop dat jullie trots op dit resultaat zijn.

Tot slot wil ik Chantal bedanken voor haar geduld en ongelimiteerde support. Ik hou van je en ik hoop dat we nog heel lang samen zullen zijn.

Rob

Curriculum Vitae

Rob Klooster werd geboren op 2 april 1983 te Almen. Het VWO-diploma werd op 29 juni 2000 behaald aan het Isendoorn College te Warnsveld.

In september 2000 werd begonnen aan de opleiding Scheikunde aan de Rijksuniversiteit Groningen. Na het afstudeeronderzoek met als onderwerp "Gradients of the Kohn–Sham energy in crystals" werd het doctoraal examen in de richting Theoretische Chemie op 31 maart 2007 succesvol afgelegd.

Gedurende de periode april 2007 tot september 2011 was hij werkzaam als assistent in opleiding (AIO) in de vakgroep Theoretische Chemie aan de Rijksuniversiteit Groningen. De resultaten van het aldaar verrichte onderzoek staan beschreven in dit proefschrift. Vanaf 1 april 2012 is hij werkzaam bij HZPC R&D te Metslawier.

